

PHASE CHEMISTRY AND PETROGENESIS OF DACITIC LAVAS FROM THE
SOUTHERN JUAN DE FUCA RIDGE

By

KEVIN RICHARD WERTS

A THESIS PRESENTED TO THE GRADUATE SCHOOL
OF THE UNIVERSITY OF FLORIDA IN PARTIAL FULFILLMENT
OF THE REQUIREMENTS FOR THE DEGREE OF
MASTER OF SCIENCE

UNIVERSITY OF FLORIDA

2012

© 2012 Kevin Werts

To Amanda

ACKNOWLEDGMENTS

I would like to thank my advisor Dr. Michael Perfit for his advice, support and guidance on this project and Dr. Matt Smith for his daily encouragements and advice. I would also like to thank Dr. Paul Mueller and Dr. Mark Panning for their helpful input and patience. The United States Geological Survey in Denver, CO, Dr. Ian Ridley and Dr. Heather Lowers are thanked for their helpfulness and support in mineral analyses. I thank the Monterey Bay Aquarium Research Institute and Dr. David Clague for providing me a unique experience on the Juan de Fuca Ridge and for teaching me about sample collection using remotely operated vehicles. I would like to acknowledge Katie Garman and Dr. Rachel Walters for their helpful discussions and advice. I would like to thank my wife, Amanda, for all of her support and understanding. The students, faculty, and staff of the geology department are all thanked for their friendship and support.

TABLE OF CONTENTS

	<u>page</u>
ACKNOWLEDGMENTS.....	4
LIST OF TABLES.....	7
LIST OF FIGURES.....	8
LIST OF ABBREVIATIONS.....	9
ABSTRACT.....	10
CHAPTER	
1 INTRODUCTION.....	12
2 BACKGROUND.....	17
Geological Setting.....	17
Previous Studies.....	18
3 ANALYTICAL METHODS.....	22
4 GLASS GEOCHEMISTRY.....	25
Basalts and Basaltic Andesites.....	25
Andesites and Dacites.....	27
5 PETROGRAPHY AND MINERAL CHEMISTRY.....	38
Basalts.....	38
Andesites and Dacites.....	38
Microphenocrysts and Phenocrysts.....	39
Pyroxene.....	39
Plagioclase.....	41
FeTi Oxides.....	42
Olivine.....	42
Accessory Phases.....	42
Crystal Clots.....	43
Basaltic Xenoliths.....	43
6 DISCUSSION.....	56
Fractional Crystallization.....	56
Evidence Supporting Magma Mixing.....	57
Mineral-Melt Equilibrium.....	59
Magma Mixing.....	61

Petrogenesis.....	64
7 CONCLUSIONS	79
LIST OF REFERENCES	80
BIOGRAPHICAL SKETCH.....	86

LIST OF TABLES

<u>Table</u>		<u>page</u>
3-1	Chemical Analyses Performed on Dive T735 Samples.	24
4-1	T735 Major Element Glass Compositions	29
4-2	T735 Trace Element Glass Compositions	31
5-1	Representative Pyroxene Analyses.....	45
5-2	Representative Plagioclase Analyses.....	46

LIST OF FIGURES

<u>Figure</u>	<u>page</u>
1-1 Map of the Juan de Fuca Ridge.....	14
4-1 Major element variation diagrams for dive T735 lavas and Cleft segment lavas.....	34
4-2 Chlorine variations in dive T735 lavas and Cleft segment lavas.....	36
4-3 Primitive mantle normalized trace element diagram.....	37
5-1 Plane polarized light images of characterized pyroxene types.....	47
5-2 Pyroxene and olivine compositions in T735 andesites and dacites.....	48
5-3 Pyroxene core to rim chemical variations.....	51
5-4 Plagioclase core to rim An# variations.....	53
5-5 Plane polarized light images of basaltic xenoliths.....	54
7-1 Major element differentiation trends for JdFR, GSC and EPR lavas.....	66
7-2 Pyroxene quadrilateral comparing T735 pyroxene trends with other tholeiitic suites.....	68
7-3 Histograms of pyroxene core and rim Mg#s.....	69
7-4 Pyroxene equilibria diagram.....	70
7-5 Olivine equilibria diagram.....	71
7-6 Mixing lines between sample G12 and various basaltic lavas.....	72
7-7 Mixing lines between sample G12 and various basaltic lavas for MgO (wt.%) vs. Al ₂ O ₃ (wt.%).....	78

LIST OF ABBREVIATIONS

AMC	Axial magma chamber
BFZ	Blanco Fracture Zone
EPR	East Pacific Rise
FTIR	Fourier transform infrared
GSC	Galapagos Spreading Center
HAM	High amplitude magnetic
ICP-MS	Inductively coupled plasma - mass spectrometry
JdFR	Juan de Fuca Ridge
LLD	Liquid line of descent
MBARI	Monterey Bay Aquarium Research Institute
MOR	Mid-ocean ridge
MORB	Mid-ocean ridge basalt
RAD	Ridge axis discontinuity
RTI	Ridge transform intersection
USGS	United States Geological Survey
wt. %	Weight percent
XRF	X-ray fluorescence

Abstract of Thesis Presented to the Graduate School
of the University of Florida in Partial Fulfillment of the
Requirements for the Degree of Master of Science

PHASE CHEMISTRY AND PETROGENESIS OF DACITIC LAVAS FROM THE
SOUTHERN JUAN DE FUCA RIDGE

By

Kevin Werts

August 2012

Chair: Michael R. Perfit
Major: Geology

Andesites, dacites and rhyodacites were collected from two constructional mounds on a series of hummocky and hooked ridges at the ridge transform intersection of the southern Juan de Fuca Ridge and Blanco Fracture Zone, during the ROV Tiburon's dive T735. Unlike other evolved lavas collected from ridge axis discontinuities which are generally aphyric, those from dive T735 are moderately phyric, containing pyroxene, plagioclase, fayalitic olivine, quartz and zircon crystals that display evidence for magma mixing. Plagioclase and pyroxene compositions span wide compositional ranges from An_{27-72} and Mg# 17-84, respectively. Whereas individual plagioclase crystals are fairly homogenous, pyroxenes show strong compositional zoning and are characterized into three types. Type 1 pyroxenes have Mg-rich cores similar to pyroxenes in ferrobasalts collected near the constructional domes. Type 2 pyroxenes have Fe-rich cores, sometimes exhibiting exsolution lamellae. Type three pyroxenes constitute the groundmass and have intermediate compositions (Mg# ~ 55) similar to rims of type 1 and 2 pyroxenes. Complex zoning in pyroxene and the presence of basaltic xenoliths with chilled margins suggests that magma mixing played a role in their evolution. The disequilibria between dacitic liquids and evolved mineral phases indicate that these

minerals were in equilibrium with a more siliceous end member magmatic composition. Mixing between an extremely fractionated basaltic andesite and a rhyolitic partial melt from a plagiogranite source explains most major elemental chemical trends and the presence of highly evolved mineral phases. However, the similarity between plagioclase and pyroxene compositions in the basaltic xenoliths and surrounding ferrobasalts suggests that a second batch of magma is responsible for their mobilization.

CHAPTER 1 INTRODUCTION

The mid-ocean ridge (MOR) system is largely dominated by tholeiitic basalts; however, it is not restricted to mafic lavas. High silica andesites, dacites and rhyodacites have been recovered from ridge axis discontinuities (RADs) in the Galapagos spreading center (GSC), East Pacific Rise (EPR) and Juan de Fuca Ridge (JdFR) (Byerly et al., 1976; Clague and Bunch, 1976; Byerly, 1980; Christie and Sinton, 1981; Fornari et al., 1983; Perfit and Fornari, 1983; Perfit et al., 1983; Langmuir et al., 1986; Regelous et al., 1999; White et al., 2009; Wanless et al., 2010) and from areas of ridge-hotspot interaction such as Iceland, the Pacific-Antarctic Ridge and Axial seamount on the JdFR (Hekinian et al., 1997; Hekinian et al., 1999; Chadwick et al., 2005; Haase et al., 2005).

Previous studies have considered lower magma supplies and/or cooler crust at RADs and the propagation of ridge tips through ridge segment ends to explain the occurrence of these high silica MOR lavas (Christie and Sinton, 1981; Sinton et al., 1983; Fornari et al., 1983; Perfit et al., 1983; Juster et al., 1989; Rubin and Sinton, 2007; Wanless et al., 2010). Extreme crystal fractionation, magma mixing, partial melting and assimilation of basaltic and/or gabbroic crust have all been hypothesized as processes that contribute to their development (Byerly et al., 1976; Byerly, 1980; Clague et al., 1981; Perfit et al., 1983; Juster et al., 1989; Hekinian et al., 1997; Haase et al., 2005; Chadwick et al., 2005; Wanless et al., 2010).

This study focuses on a wide compositional range of lavas that were collected in 2004, using the ROV Tiburon during a cruise of the Monterey Bay Aquarium Research Institute (MBARI) to the southern end of the JdFR. Highly evolved mid-ocean ridge

basalt (MORB), andesite, dacite and rhyodacite were sampled during dive T735 at the ridge-transform intersection (RTI) between the southern Cleft segment of the JdFR and the Blanco Fracture Zone (BFZ) (Figure 1-1). The moderately phyric nature of dacitic lavas from dive T735 make this sample set unique among those previously investigated from a RAD (e.g. 85°W and 95°W RTI on the GSC and 9°N OSC on the EPR). Basaltic xenoliths and the presence of highly evolved mineral phases indicate that the petrogenetic history of the dacites may be more complex than their glass chemistry alone suggests. This study aims to further assess the processes involved in the petrogenesis of MOR dacites at RADs using the petrography and phase chemistry of lavas collected from dive T735 on the southern JdFR.

A

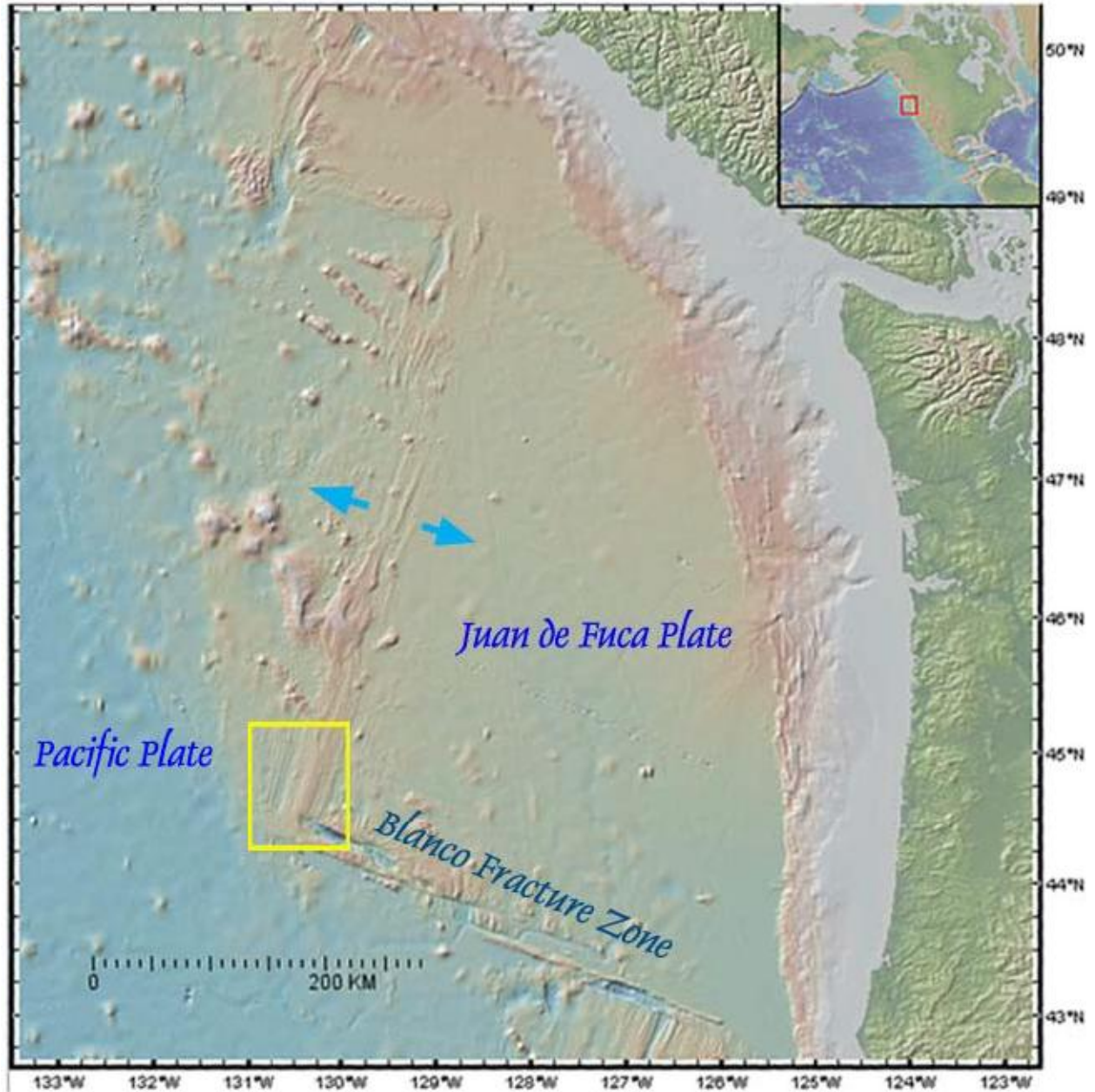


Figure 1-1. Map of the Juan de Fuca Ridge and T735 dive area. A) Map of the entire Juan de Fuca Ridge, the yellow box indicates the general location of samples collected from dive T735 and the location of image B. B) Hooked and curved ridges at the ridge-transform intersection. The yellow box indicates the general location of image C. C) Locations of samples collected on dive T735.

B

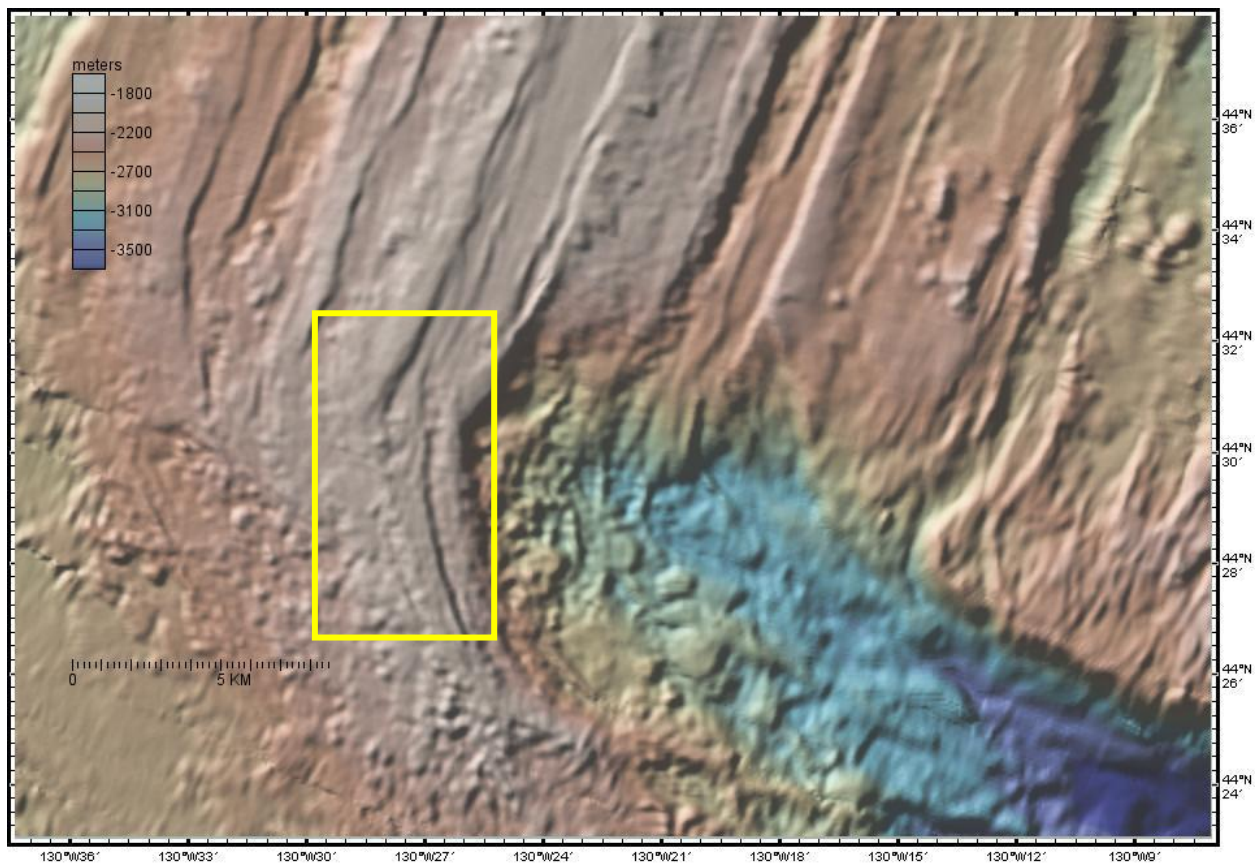


Figure 1-1. Continued

DIVE T735 (Cleft Dive #1) -- AUGUST 31, 2004

C

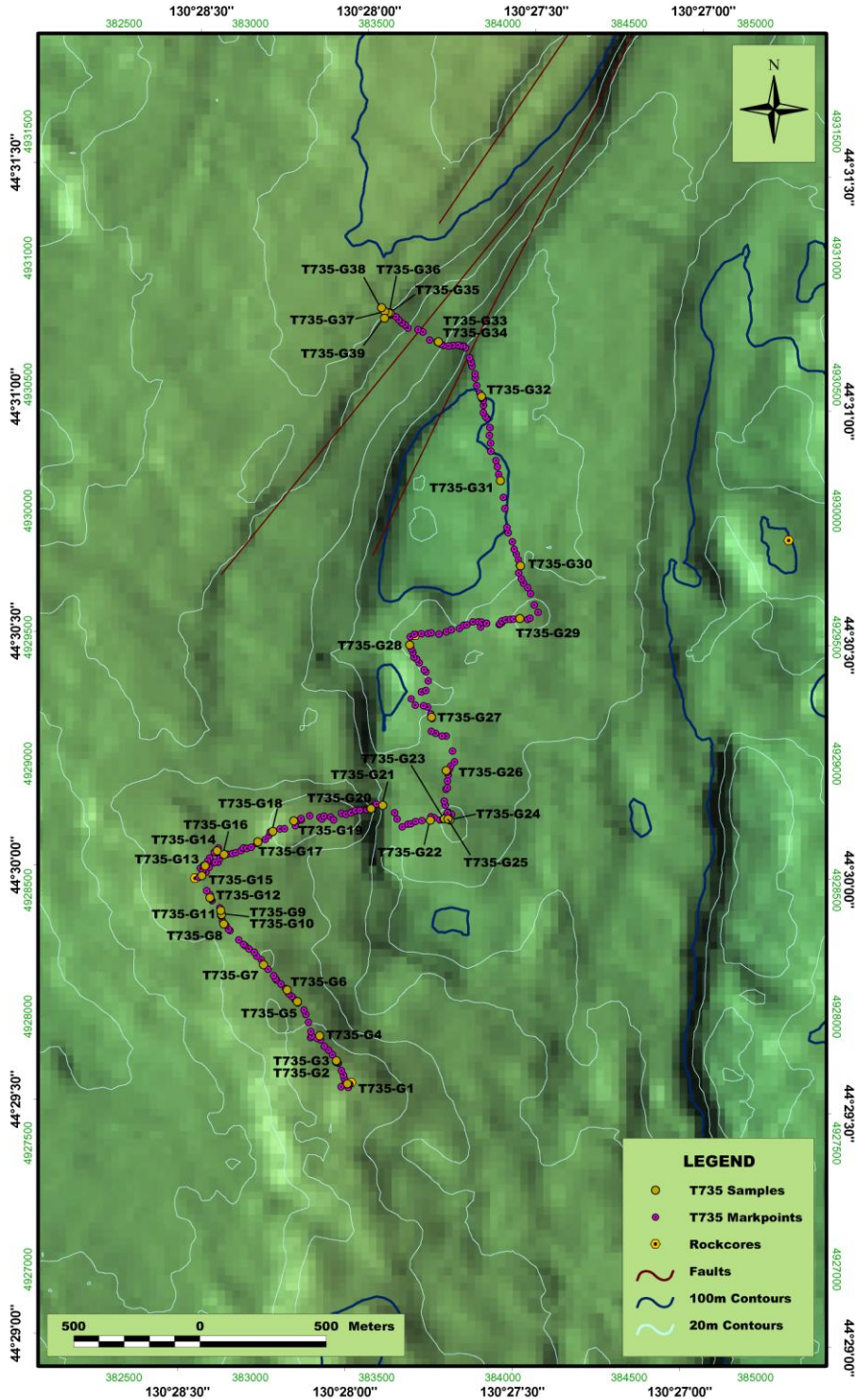


Figure 1-1. Continued

CHAPTER 2 BACKGROUND

Geological Setting

The intermediate spreading-rate (~ 6 cm/yr full rate) Juan de Fuca spreading center is located off the coasts of Washington and Oregon, extending from the Sovanco fracture zone (48°50`N) to its southern terminus, the Blanco Fracture Zone (BFZ) (44°27`N) (Vine and Wilson, 1965; Raff and Mason, 1961; Wilson, 1965, Kappel and Ryan 1986). Seven second-order ridge segments (West Valley, Endeavour, Cobb, CoAxial, Axial, Vance, and Cleft) make up the JdFR from north to south, respectively (Delaney et al. 1981; Normark et al. 1983; Embley et al., 1983; Crane et al., 1985; Kappel and Ryan, 1986; Embley et al., 1990).

The Cleft segment extends from 45°03`N to 44°27`N where it intersects the BFZ along its southern end (Embley et al., 1983; Embley et al. 1991; Smith et al., 1994). A 3 km wide axial valley hosts an axial summit collapse trough or fissure known as the “cleft”, which is 30 to 90 m wide, and ~ 10-15 m deep, extending from 44°44` to 44°35`N (Normark et al., 1986; Normark et al., 1987; Embley et al., 1991; Stakes et al., 2006). Seismic reflection profiles have imaged an axial magma chamber (AMC) reflector that is present beneath 60% of the Cleft segment but is absent north of 45°01`N and south of 44°38`N (Canales et al., 2005; Stakes et al., 2006). Lavas collected from the southern end of the Cleft are generally more evolved (lower MgO wt.%) than those collected from its northern end (Sinton et al., 1983; Smith et al., 1994; Stakes et al., 2006). The evolved nature of the southern Cleft lavas is in agreement with the absence of an AMC reflector beneath the majority of the southern portion of the Cleft segment, suggesting that more crystalline or “mushy” zones and lower temperatures may prevail in the south,

relative to the north (Sinton and Detrick, 1992; Smith et al., 1994; Perfit and Chadwick, 1998; Stakes et al., 2006).

A series of 16 dives using the ROV Tiburon investigated the geologic, morphologic and magnetic characteristics of the Cleft segment from 2000-2004 (Stakes et al., 2006). Among these dives was dive T735, which examined the southern terminus of the Cleft segment and a series of hummocky and hooked ridges that extend south of the RTI and appear to have formed by magmatic propagation through the BFZ into older and cooler crust generated by the Gorda ridge (Embley and Wilson, 1992; Cotsonika, 2006; Stakes et al., 2006; Wanless et al. 2010). Two constructional domes ranging from 20-30 m in height and 200-500 m in width were sampled along these hooked ridges, the compositions of which range from high-silica andesite to rhyodacite (62.2-66.9 wt.% SiO₂) (Cotsonika, 2006; Stakes et al., 2006; Wanless et al., 2010; Schmitt et al., 2011). Surrounding the andesitic-rhyodacitic domes are ferrobasalts and FeTi basalts that are similar in composition to other lavas collected from the Cleft segment (Stakes et al., 2006; Schmitt et al., 2011). A more detailed account of the geology and tectonics of the Cleft segment and dive T735 is presented by Stakes et al. (2006).

Previous Studies

Vogt and Johnson (1973) predicted the occurrence of Fe and Ti rich basalts along the GSC based on the presence of high amplitude magnetic (HAM) anomalies. This hypothesis led Byerly et al. (1976) to test whether FeTi rich basalts were present along HAM zones in the GSC and to the discovery of MOR andesites and dacites. Since then, a number of studies have focused on the processes of differentiation responsible for the production of these high silica MOR lavas (Byerly et al., 1976; Byerly, 1980; Clague et

al., 1981; Perfit et al., 1983; Juster et al., 1989; Hekinian et al., 1997; Haase et al., 2005; Wanless et al., 2010).

Christie and Sinton (1981) suggested that the occurrence of evolved MOR lavas along the GSC at 95°W was due to the propagation of the ridge segment through a ridge-transform intersection. They hypothesized that propagation of a ridge through older and cooler lithosphere would lead to increased cooling rates and thus more extreme crystal fractionation. Low-pressure fractional crystallization has been further substantiated by others (Byerly et al., 1976; Clague and Bunch, 1976; Schilling et al., 1976; Byerly, 1980; Fornari et al., 1983; Perfit and Fornari, 1983; Perfit et al., 1983) as the dominant differentiation process in the development of evolved lavas at 85°W and 95°W on the GSC. In order to produce andesitic–rhyodacitic lavas, 75-87% fractional crystallization of a MORB parent is required (Byerly, 1980; Clague et al., 1981; Perfit et al., 1983). However, closed-system fractionation is unable to explain the observed incompatible trace element enrichments and increasing Ce/Yb ratios in the 85°W and 95°W GSC lavas (Perfit et al. 1983). Therefore, small extents of open-system behavior such as magma mixing or crustal assimilation may be required to account for these discrepancies.

An alternative to extreme crystal fractionation in the production of MOR dacites is partial melting of oceanic crust. Experimental studies have demonstrated that dacitic melts can be produced by partial melting of hydrated gabbroic or basaltic crust at temperatures of 850-900°C and <10% melting (Beard and Lofgren, 1991; Koepke et al., 2004; Kvassnes and Grove, 2008; Wanless et al., 2010). Assimilation and partial melting of altered oceanic crust has been proposed to account for low Nb/La and high

Cl/K ratios observed in andesites from the Pacific-Antarctic ridge and in dacites from the EPR, GSC and JdFR (Haase et al., 2005; Wanless et al., 2010). Using energy constrained-assimilation fractional crystallization models, Wanless et al. (2010) demonstrated that major and trace element compositions of dacites from the 9°N OSC on the EPR can be reproduced by >75% crystallization of a MORB parent magma and 5-20% assimilation of altered amphibole bearing oceanic crust. Wanless et al. (2010) also noted the strong similarities between major and trace element compositions of dacites from 9°N on the EPR with those from 85°W on the GSC and those discussed in this study from dive T735 on the JdFR, suggesting that their models may also be applicable to these suites.

Models describing the petrogenesis of MOR dacites (i.e. crystal fractionation, partial melting and assimilation of hydrated oceanic crust) have largely been based on glass chemistry. However, petrographic evidence from each of these suites suggests that a more complicated history involving magma mixing may have played an important role in their development. Basaltic xenoliths are ubiquitous in dacites from the 85°W and 95°W GSC, 9°N EPR and from dive T735 on the JdFR with rarer high silica xenoliths composed of plagioclase, quartz, and rhyolitic glass occurring in dacites from the GSC and JdFR (Byerly et al., 1976; Perfit et al., 1983; Cotsonika, 2006;). Secondly, pyroxenes from the GSC and JdFR dacites display both normal and reverse zoning, implying earlier crystallization in magmas that were more mafic or felsic than their host glass. Glass inclusions in plagioclase from the 85°W GSC dacites have also been used to support magma mixing. For example, plagioclase xenocrysts in basaltic andesites contain FeTi basalt glass inclusions while those in andesites contain higher silica glass

inclusions, suggesting that the crystals originated in magmas that were either more mafic or felsic than their host glass (Perfit et al. 1983).

CHAPTER 3 ANALYTICAL METHODS

Thirty-nine lava samples were collected on dive T735, which explored the constructional volcanic terrain at the ridge transform intersection of the southern JdFR with the Blanco Fracture Zone. Glassy quenched rims of all samples were analyzed for major elements. Whole rock and mineral chemistry were also measured for a representative group of samples. Table 3-1 provides a complete list of analyses performed for each of the thirty-nine samples collected.

Major and minor elements were determined for glass and mineral samples using a JEOL 8900 Electron Microprobe. Minerals phases were analyzed on polished thin-sections and natural glasses were analyzed on fresh, hand-picked separates mounted and polished on glass slides. Care was taken to collect crystal-free chips that were ultrasonically cleaned in a solution made from equal parts 2.5N reagent grade HCl and 30% H₂O₂ to remove any surficial coatings (Cotsonika, 2006). Microprobe analyses were performed at the United States Geological Survey (USGS) in Denver, CO and Florida International University on four separate occasions from 2004 to 2012. On each occasion, USGS mineral standards were used to calibrate the microprobe analyses and secondary normalizations were completed using University of Florida glass standard 2392-2 and USGS standard glass GSC that also served as drift monitors during analysis. An accelerating voltage of 15 keV, beam current of 20 nA and a beam diameter of 20 µm were used for glass analyses. Mineral analyses were performed with a beam diameter of 1 µm. Replicate analyses of standard glasses indicate that the analytical precision of major elements in glasses with concentration greater than 1 wt%

is precise to within 1 to 4 relative percent but becomes significantly greater (10-20%) with abundances below 0.2 wt%.

Trace element contents of crystal free glass chips were analyzed at the University of Florida using an Element2 inductively coupled plasma - mass spectrometer at medium resolution. USGS rock standards were used for calibration and University of Florida MORB standards 2392-2 and ENDV were used as drift monitors and to check for internal precision. Replicate analyses of USGS standard BHVO-1 indicate the accuracy and precision for all elements is equal to or better than ± 5 relative percent. A more detailed discussion of sample preparation, dissolution procedures, standards and errors can be found in Cotsonika (2006) and Goss et al. (2010).

Some of the more crystalline sections of dacitic samples with substantial crystal and xenolith contents were analyzed by traditional X-Ray Fluorescence techniques at Geo labs in Ottawa, Canada. A representative subset of thirteen glass samples was selected for volatile analyses (Table 3-1). Samples were analyzed for H₂O and CO₂ concentrations by Fourier transform infrared (FTIR) spectroscopy at the University of Oregon using methods described in Johnson et al. (2009) and Wanless et al (2011).

Table 3-1. Chemical Analyses Performed on Dive T735 Samples. Glass major and mineral = electron microprobe, glass trace = Element2 ICP-MS, whole rock = XRF, volatiles = FTIR spectroscopy

Sample	G1	G2	G3	G4	G5	G6	G7	G8
Glass-Major	✓	✓	✓	✓	✓	-	✓	✓
Glass-Trace	-		✓	✓	-	-	✓	✓
Whole Rock	-	✓	-	-	-	-	✓	-
Volatiles	-	-	-	-	-	-	-	-
Minerals	-	-	-	-	-	-	-	-
	G9	G10	G11	G12	G13	G14	G15	G16
Glass-Major	✓	✓	✓	✓	✓	✓	✓	✓
Glass-Trace	✓	✓	✓	✓	✓	✓	✓	✓
Whole Rock	✓	-	✓	✓	-	-	-	✓
Volatiles	✓	✓	✓	✓	✓	✓	✓	✓
Minerals	✓	✓	✓	✓	✓	✓	✓	✓
	G17	G18	G19	G20	G21	G22	G23	G24
Glass-Major	✓	✓	✓	✓	✓	✓	✓	✓
Glass-Trace	✓	✓	✓	✓	✓	✓	-	-
Whole Rock	✓	-	✓	-	-	-	✓	-
Volatiles	-	✓	✓	✓	-	-	✓	-
Minerals	✓	✓	✓	✓	-	-	✓	-
	G25	G26	G27	G28	G29	G30	G31	G32
Glass-Major	✓	✓	✓	✓	✓	✓	✓	✓
Glass-Trace	-	-	-	✓	✓	-	-	✓
Whole Rock	-	-	-	-	-	-	-	-
Volatiles	-	-	-	-	-	-	-	-
Minerals	-	-	-	-	-	-	-	✓
	G33	G34	G35	G36	G37	G38	G39	
Glass-Major	-	✓	✓	✓	✓	✓	-	
Glass-Trace	-	-	✓	-	-	-	-	
Whole Rock	-	-	-	-	-	-	-	
Volatiles	-	-	✓	-	-	-	-	
Minerals	-	-	-	-	-	-	-	

CHAPTER 4 GLASS GEOCHEMISTRY

Samples collected from dive T735 are discussed here in the context of those previously analyzed from the Cleft suite, which has been extensively sampled both on and off axis (Smith et al., 1994; Stakes et al, 2006). Basaltic lavas from the Cleft suite are normal, incompatible element-depleted MORB with MgO values ranging from 8.1 wt.% in the most primitive basalts to 3.8 wt.% in the more evolved basaltic andesites. A strong correlation between distance along the ridge and MgO values of Cleft lavas has previously been cited, generally decreasing from north to south (Smith et al., 1994; Stakes et al. 2006)

Major element variations of the Cleft suite resemble typical tholeiitic differentiation trends (Figure 4-1). Decreasing values of MgO are associated with increasing values of TiO_2 , FeO^{T} (total FeO as Fe^{2+}), Na_2O , K_2O and P_2O_5 and decreasing values of SiO_2 , Al_2O_3 , and CaO in the basaltic lavas (Figure 4-1). The trends are typically smooth; however, significant deviations from the curvilinear paths and greater variability occur in SiO_2 , TiO_2 , FeO^{T} , Al_2O_3 , Na_2O , K_2O and P_2O_5 at ~ 6 to 4 MgO wt.% in basaltic lavas from Stakes et al. (2006). These inflections vary from the original curvilinear paths in the following ways: (1) values of SiO_2 , Al_2O_3 , and K_2O are higher at a given MgO (2) values of FeO^{T} , TiO_2 , Na_2O and P_2O_5 are lower at a given MgO and (3) inflections of each oxide diverge toward lower MgO values or in the direction of the compositions of T735 andesites and dacites (Figure 4-1).

Basalts and Basaltic Andesites

Basalts and ferrobasalts from dive T735 span a limited range of compositions in comparison to the entire Cleft suite (Table 4-1). The MgO values (6.29-7.55 wt%) are

intermediate, falling between the most primitive and evolved samples collected from the Cleft. Most major and minor elements (SiO_2 , CaO , Na_2O , K_2O , P_2O_5 , and MnO) do not vary greatly at given MgO values. Two exceptions to this are FeO^{T} and TiO_2 , which span a broad range from 11.3 – 12.9 wt.% and 1.67-2.26 wt.% respectively at ~7 wt% MgO . Most major element oxides of dive T735 basalt samples plot centrally within the LLD defined by the entire Cleft suite at a given MgO . However, Al_2O_3 and TiO_2 plot above and below other Cleft suite samples respectively, at a given MgO value.

The major element variations of basaltic lavas can be modeled by relatively large amounts (> 55%) of low-pressure (<100 MPa) fractional crystallization of a relatively primitive melt (Smith et al. 1994; Tierney, 2003; Stakes et al. 2006). Decreasing values of Al_2O_3 with decreasing values of MgO coupled with increasing values of $\text{CaO}/\text{Al}_2\text{O}_3$ suggest that plagioclase or plagioclase + olivine were the first phases in the crystallization sequence (Smith et al. 1994; Cotsonika, 2006). Clinopyroxene likely begins to fractionate at ~7.5 wt% MgO , when $\text{CaO}/\text{Al}_2\text{O}_3$ begins to decrease (Smith et al. 1994; Cotsonika, 2006).

Volatiles (H_2O and CO_2) were analyzed from two basalts collected on dive T735. Samples T735-G23 and T735-G35 have H_2O values of 0.27 and 0.17 wt% and CO_2 values of 118 and 101 ppm, respectively. Chlorine contents in these two samples and those collected by Smith et al. (1994) are less than 0.05 wt.%. The more evolved basaltic lavas ($\text{MgO} < \sim 6$ wt.%) collected by Stakes et al. (2006) have significantly higher values, up to 0.31 wt.%, that increase with decreasing MgO (Figure 4-2a). Values of $\text{Cl}/\text{K}_2\text{O}$ in T735 basalts vary between 0.05 and 0.23 wt.%, increasing with decreasing MgO values (Figure 4-2b).

Trace element values in T735 basalt samples (Table 4-2) are similar to those in differentiated basalts from the Cleft segment (Smith et al., 1994). They are typical normal-incompatible element depleted MORB with negative Sr and Eu anomalies on primitive mantle normalized diagrams (Figure 4-3). Trace elements from T735 basalts show variations similar to those described by Smith et al. 1994, but extent to lower MgO values.

Andesites and Dacites

Dive T735 andesites and dacites appear to extend the tholeiitic differentiation trends to low MgO (1.94-0.6 wt.%) and high SiO₂ (62-67 wt.%) compositions. However, a clear break in the data set occurs between 2 to 3.8 wt.% MgO (Figure 4-1). Major element variations of SiO₂, CaO, Na₂O, K₂O and CaO/Al₂O₃ follow and extend the trends defined by the basaltic lavas, whereas, TiO₂, FeO^T, and P₂O₅ have marked inflection points, decreasing in abundance with decreasing MgO (Figure 4-1). The Al₂O₃ trends in samples containing ~ 0 to 2 wt.% MgO generally parallel those from ~ 4.5 to 6.5 wt.% MgO. Whole rock Al₂O₃ values for the evolved lavas are significantly lower than their corresponding glass values and appear to follow the same curvilinear path produced by the basaltic glasses.

Water and CO₂ concentrations were determined in a number of evolved samples (Table 4-1). Values of H₂O and CO₂ range from 0.35 to 2.0 wt.% and 0.28 ppm to below detection limits, respectively. Lower values of CO₂ are likely related to degassing, given the highly vesicular nature of the samples, whereas higher concentrations of H₂O may either be related to increasing degrees of evolution or to assimilation of hydrated crustal material (Wanless et al. 2011). Chlorine concentrations range from 0.41 to 0.61 wt.% (Figure 4-2a). This extends the curvilinear trend in Figure 4-2a to values over 12 times

that measured in the most chlorine rich T735 basalt. The Cl/K₂O values are lower (0.4 to 0.5 wt.%) than those of several of the basaltic andesites from Stakes et al. (2006) which approach values of 0.8 wt.% (Figure 4-2b).

Evolved lavas exhibit increased incompatible trace element abundances with decreasing MgO values (Figure 4-3). However, Sr values are similar to those of the basalts, showing little change with fractionation and thus producing large negative Sr anomalies on mantle normalized diagrams. There are generally no crossing patterns indicating the lavas may be related by fractional crystallization (Figure 4-3). Sample G20 however, does exhibit crossing patterns in Zr and Eu which have similar values with the two andesites, G18 and G19.

Table 4-1. T735 Major Element Glass Compositions

Sample	SiO ₂	TiO ₂	Al ₂ O ₃	FeO ^T	MnO	MgO	CaO	Na ₂ O	K ₂ O	P ₂ O ₅	Cl	Total (wt.%)	H ₂ O	CO ₂ (ppm)
G1	50.48	2.12	13.31	12.31	0.21	6.87	11.27	2.53	0.17	0.22	0.02	99.81	-	-
G2	50.39	2.06	13.32	12.30	0.20	7.04	11.18	2.51	0.17	0.22	0.02	99.69	-	-
G3	50.42	2.12	13.33	12.32	0.21	6.94	11.17	2.54	0.17	0.20	0.02	99.74	-	-
G4	50.59	1.87	13.48	11.96	0.22	6.86	11.25	2.69	0.18	0.23	0.03	99.68	-	-
G5	50.47	2.09	13.38	12.21	0.20	6.94	11.24	2.56	0.17	0.22	0.02	99.80	-	-
G7	50.48	2.12	13.12	12.29	0.20	6.78	11.17	2.52	0.17	0.24	0.03	99.41	-	-
G8	50.38	2.10	13.13	12.22	0.20	6.92	11.13	2.54	0.17	0.21	0.02	99.33	-	-
G9	63.73	1.20	12.42	9.45	0.17	1.04	4.39	4.76	1.14	0.33	0.55	99.47	1.86	↓ det
G10	63.98	1.17	12.43	9.35	0.17	1.00	4.29	4.76	1.15	0.33	0.55	99.48	1.96	↓ det
G11	63.36	1.22	12.38	9.87	0.19	1.03	4.43	4.79	1.10	0.40	0.51	99.56	1.73	↓ det
G12	66.89	0.81	12.23	7.95	0.14	0.60	3.41	5.01	1.30	0.18	0.61	99.44	1.98	↓ det
G13	62.82	1.39	12.35	9.81	0.16	1.40	4.85	4.52	1.09	0.34	0.52	99.55	1.63	↓ det
G14	62.90	1.33	12.36	9.80	0.19	1.38	4.80	4.57	1.08	0.37	0.53	99.59	0.35	224.88
G15	62.70	1.33	12.33	10.25	0.19	1.15	4.60	4.76	1.07	0.42	0.49	99.58	2.00	↓ det
G16	66.43	0.85	12.44	8.02	0.16	0.60	3.57	5.07	1.28	0.30	0.61	99.63	1.77	↓ det
G17	64.33	1.21	12.56	9.16	0.18	0.76	4.03	5.04	1.17	0.35	0.55	99.63	-	-
G18	62.16	1.26	13.32	8.89	0.16	1.94	5.40	4.36	1.02	0.18	0.41	99.43	1.97	↓ det
G19	61.95	1.34	13.59	8.94	0.16	1.73	5.38	4.62	1.03	0.17	0.42	99.65	2.01	↓ det
G20	65.75	0.98	12.88	7.28	0.12	1.33	4.32	4.71	1.28	0.11	0.52	99.60	1.51	↓ det
G21	50.63	2.26	12.89	12.70	0.22	6.68	11.11	2.58	0.18	0.25	0.02	99.80	-	-
G22	50.09	2.22	12.77	12.79	0.22	6.69	11.03	2.62	0.16	0.23	0.03	99.12	-	-

Table 4-1. Continued

Sample	SiO ₂	TiO ₂	Al ₂ O ₃	FeOT	MnO	MgO	CaO	Na ₂ O	K ₂ O	P ₂ O ₅	Cl	Total (wt.%)	H ₂ O	CO ₂ (ppm)
G23	50.53	2.19	13.02	12.66	0.22	6.74	11.17	2.62	0.16	0.23	0.02	99.85	0.27	117.74
G24	50.54	2.22	12.91	12.78	0.21	6.67	11.11	2.57	0.17	0.23	0.02	99.72	-	-
G25	50.46	2.22	13.02	12.72	0.22	6.68	11.10	2.63	0.17	0.2	0.03	99.73	-	-
G26	50.65	2.18	13.08	12.64	0.23	6.92	11.19	2.6	0.16	0.22	0.02	100.16	-	-
G27	50.46	2.13	13.05	12.44	0.24	7.05	11.19	2.53	0.16	0.19	0.02	99.76	-	-
G28	50.47	2.13	13.11	12.42	0.22	7.13	11.20	2.54	0.15	0.2	0.02	99.88	-	-
G29	50.64	2.13	13.04	12.90	0.24	6.82	10.94	2.62	0.16	0.23	0.02	100.02	-	-
G30	50.66	2.11	12.93	12.58	0.21	6.69	10.86	2.57	0.17	0.2	0.02	99.28	-	-
G31	51.57	1.67	13.38	11.30	0.20	6.78	10.98	2.65	0.2	0.16	0.04	99.22	-	-
G32	50.32	2.15	12.81	12.77	0.24	6.29	10.92	2.63	0.15	0.21	0.02	98.78	-	-
G34	50.46	1.61	13.60	10.78	0.19	7.43	11.81	2.45	0.12	0.16	0.01	98.93	-	-
G35	50.67	1.61	13.76	10.86	0.19	7.55	11.84	2.47	0.12	0.14	0.01	99.54	0.17	101.00
G37	50.67	2.11	13.05	12.76	0.23	6.68	10.95	2.63	0.15	0.18	0.02	99.71	-	-
G38	50.72	2.09	13.05	12.69	0.22	6.70	10.94	2.61	0.15	0.18	0.02	99.66	-	-

Table 4-2. T735 Trace Element Glass Compositions

Sample	Sc	V	Cr	Co	Ni	Cu	Zn	Ga	Rb	Sr	Y
G2	41.2	382	173	37.6	57.2	55.4	99.2	18.0	1.2	102	50.4
G4	42.0	340	188	38.0	53.8	64.8	89.2	17.4	1.2	118	44.2
G5	41.8	391	180	38.5	59.7	56.2	101.9	18.3	1.2	104	51.2
G7	40.4	378	170	37.2	57.4	54.8	98.3	17.6	1.2	100	49.7
G8	41.1	384	173	37.8	59.3	55.0	99.7	18.0	1.2	102	50.4
G9	18.1	73	5	12.6	4.5	15.9	137.9	26.6	10.3	86	214.7
G10	21.1	109	21	15.9	10.4	23.2	136.2	25.9	9.4	90	197.2
G11	20.1	67	4	13.6	3.4	15.9	152.3	28.0	10.6	93	230.0
G12	15.9	48	2	10.0	1.7	13.5	144.5	27.6	12.0	80	240.4
G13	19.6	110	11	14.9	7.9	18.7	134.3	25.8	10.3	86	202.6
G14	19.9	113	11	15.2	8.0	19.0	134.6	26.1	10.1	87	201.2
G15	19.5	71	7	13.9	4.3	15.4	146.0	27.3	9.9	93	212.6
G16	16.1	48	3	10.4	2.2	13.6	144.4	27.8	11.8	82	238.8
G17	18.2	66	6	12.3	3.7	14.2	142.4	27.2	10.7	88	220.0
G18	22.6	178	44	19.1	18.9	27.5	116.1	23.3	9.4	79	160.0
G19	23.4	180	54	19.7	20.4	27.9	116.7	23.1	9.2	79	158.4
G20	17.1	123	32	14.1	13.8	21.7	113.4	24.3	12.7	67	194.2
G21	41.5	391	152	38.8	58.5	54.8	102.3	18.2	1.3	102	52.9
G22	41.1	389	148	38.2	55.2	54.7	102.7	18.2	1.3	102	53.4
G23	42.0	395	159	38.4	54.7	55.5	103.0	18.6	1.3	105	53.1
G28	41.6	392	169	38.0	55.9	55.0	100.7	18.3	1.2	104	51.7
G29	41.1	388	101	38.3	45.6	53.6	103.4	18.3	1.3	109	52.3
G32	40.7	392	98	39.1	46.5	53.5	105.2	18.5	1.1	101	51.7
G35	40.5	330	287	38.0	70.0	63.3	84.7	16.6	0.7	101	37.6

Table 4-2. Continued

Sample	Zr	Nb	Ba	La	Ce	Pr	Nd	Sm	Eu	Gd	Tb
G2	135.8	4.47	15.10	4.93	15.69	2.51	13.80	4.68	1.51	5.46	1.17
G4	125.1	4.34	16.69	4.75	14.74	2.36	12.59	4.18	1.36	4.73	1.04
G5	136.9	4.59	15.44	5.02	15.94	2.54	13.99	4.72	1.52	5.51	1.19
G7	133.9	4.42	14.92	4.87	15.47	2.48	13.46	4.55	1.47	5.34	1.15
G8	134.7	4.49	16.23	4.98	15.63	2.49	13.78	4.64	1.48	5.34	1.17
G9	637.2	19.29	82.57	29.97	82.13	11.33	64.59	18.89	3.94	20.89	4.46
G10	585.3	17.40	77.40	26.79	74.50	10.43	59.10	17.38	3.67	19.08	4.11
G11	672.0	20.10	87.69	30.59	84.39	11.84	68.05	20.19	4.20	22.01	4.75
G12	663.7	21.20	95.39	33.78	91.20	12.79	72.82	21.15	4.15	23.23	4.99
G13	590.1	17.82	83.83	28.28	77.50	10.80	61.17	17.96	3.67	19.72	4.20
G14	580.3	17.72	79.17	28.15	77.34	10.74	61.05	17.73	3.65	19.55	4.16
G15	636.4	18.62	78.15	29.13	80.08	11.22	64.26	18.89	4.10	20.77	4.43
G16	671.6	21.01	93.54	33.47	91.83	12.60	71.67	20.97	4.14	22.82	4.91
G17	641.9	19.47	84.95	30.18	83.32	11.59	66.59	19.47	4.05	21.31	4.55
G18	440.8	14.09	70.55	22.60	61.40	8.51	47.36	13.86	2.81	15.10	3.27
G19	439.8	13.96	69.20	22.36	60.66	8.41	46.82	13.76	2.79	14.96	3.24
G20	396.8	17.03	88.70	29.38	78.75	10.71	59.18	16.98	3.01	18.40	3.97
G21	140.9	4.68	16.25	5.21	16.28	2.60	14.31	4.78	1.52	5.48	1.20
G22	142.0	4.76	16.50	5.24	16.39	2.61	14.55	4.87	1.54	5.52	1.21
G23	142.3	4.71	15.99	5.17	16.28	2.61	14.48	4.86	1.53	5.51	1.21
G28	137.8	4.59	16.17	5.06	15.89	2.54	14.01	4.73	1.50	5.38	1.19
G29	142.0	4.68	16.48	5.19	16.44	2.63	14.40	4.82	1.53	5.49	1.19
G32	134.3	4.14	14.65	4.67	15.04	2.44	13.52	4.64	1.48	5.34	1.18
G35	101.7	2.88	11.21	3.40	11.43	1.92	9.98	3.49	1.18	4.00	0.88

Table 4-2. Continued

Sample	Dy	Ho	Er	Tm	Yb	Lu	Hf	Ta	Pb	Th	U
G2	7.74	1.80	5.13	0.69	4.97	0.77	3.80	0.284	0.372	0.270	0.111
G4	6.78	1.56	4.37	0.61	4.34	0.67	3.40	0.241	0.349	0.268	0.105
G5	7.82	1.83	5.21	0.70	5.01	0.77	3.83	0.280	0.373	0.276	0.111
G7	7.57	1.77	5.01	0.67	4.83	0.75	3.72	0.275	0.361	0.268	0.109
G8	7.66	1.79	5.11	0.68	4.94	0.76	3.73	0.269	0.397	0.272	0.112
G9	29.37	7.19	21.99	2.46	20.64	3.19	18.32	1.273	2.480	2.818	1.067
G10	27.02	6.61	20.16	2.29	19.23	2.97	16.83	1.142	2.291	2.544	0.970
G11	31.08	7.67	23.25	2.59	22.00	3.41	19.06	1.346	2.627	2.830	1.074
G12	32.88	8.09	24.87	2.78	23.63	3.65	19.62	1.450	2.915	3.285	1.240
G13	27.73	6.81	20.82	2.35	19.92	3.08	17.18	1.217	3.105	2.796	1.054
G14	27.59	6.77	20.67	2.34	19.55	2.99	16.77	1.165	2.347	2.725	1.030
G15	29.32	7.14	21.87	2.46	20.71	3.16	18.21	1.230	2.430	2.629	1.017
G16	32.59	8.02	24.58	2.75	23.37	3.56	19.71	1.398	2.850	3.208	1.214
G17	30.13	7.40	22.67	2.55	21.52	3.29	18.68	1.302	2.590	2.850	1.089
G18	21.69	5.31	16.26	1.88	15.73	2.40	13.00	0.962	2.141	2.325	0.866
G19	21.56	5.29	16.13	1.86	15.57	2.38	12.96	0.927	2.075	2.287	0.851
G20	26.49	6.53	19.96	2.29	19.15	2.90	13.10	1.169	2.739	3.140	1.148
G21	7.95	1.86	5.26	0.70	5.16	0.80	3.89	0.274	0.398	0.287	0.118
G22	8.01	1.88	5.33	0.71	5.22	0.81	3.92	0.293	0.406	0.290	0.118
G23	8.02	1.87	5.31	0.70	5.21	0.81	3.89	0.271	0.389	0.285	0.117
G28	7.79	1.82	5.21	0.69	5.07	0.79	3.76	0.266	0.389	0.279	0.114
G29	7.94	1.85	5.22	0.70	5.16	0.79	3.89	0.275	0.414	0.287	0.115
G32	7.76	1.83	5.22	0.69	5.07	0.79	3.73	0.237	0.371	0.250	0.100
G35	5.88	1.35	3.73	0.54	3.72	0.58	2.82	0.150	0.248	0.173	0.069

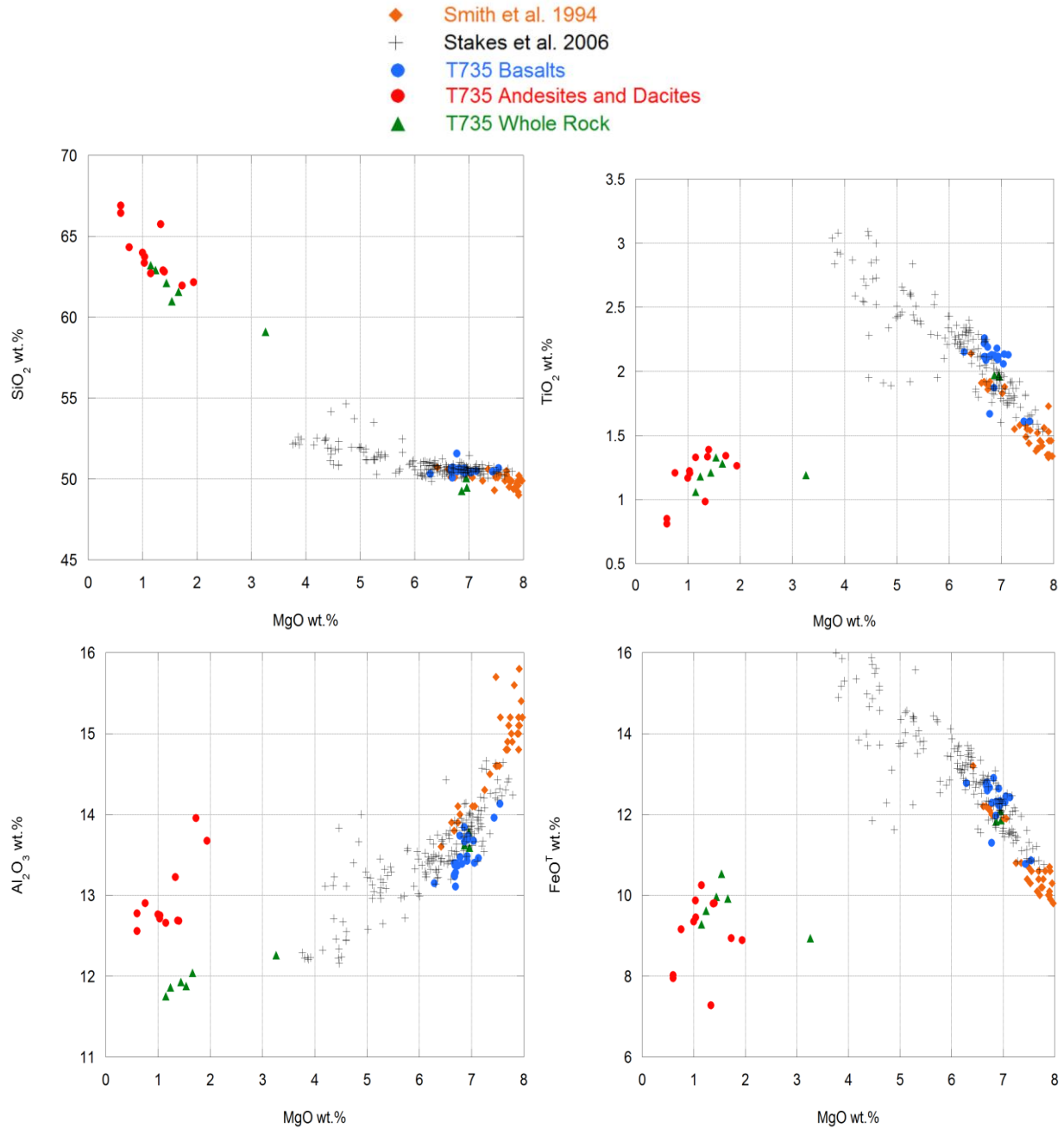


Figure 4-1. Major element variation diagrams for dive T735 lavas and Cleft segment lavas from Smith et al. 1994 and Stakes et al. 2006. MgO is plotted against A) SiO₂ B) TiO₂ C) Al₂O₃ D) FeO(t) E) CaO F) Na₂O G) K₂O and H) P₂O₅

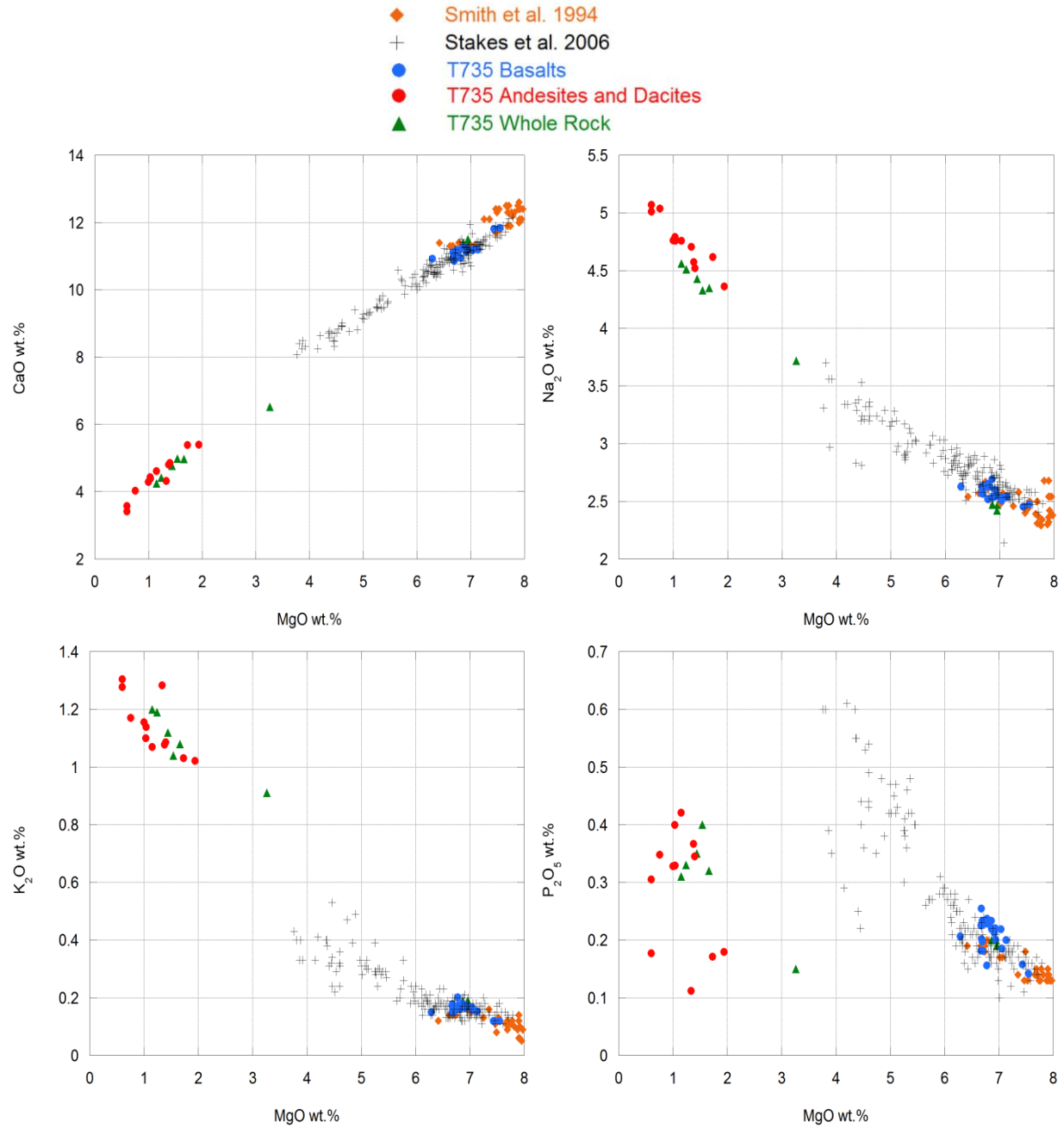


Figure 4-1. Continued

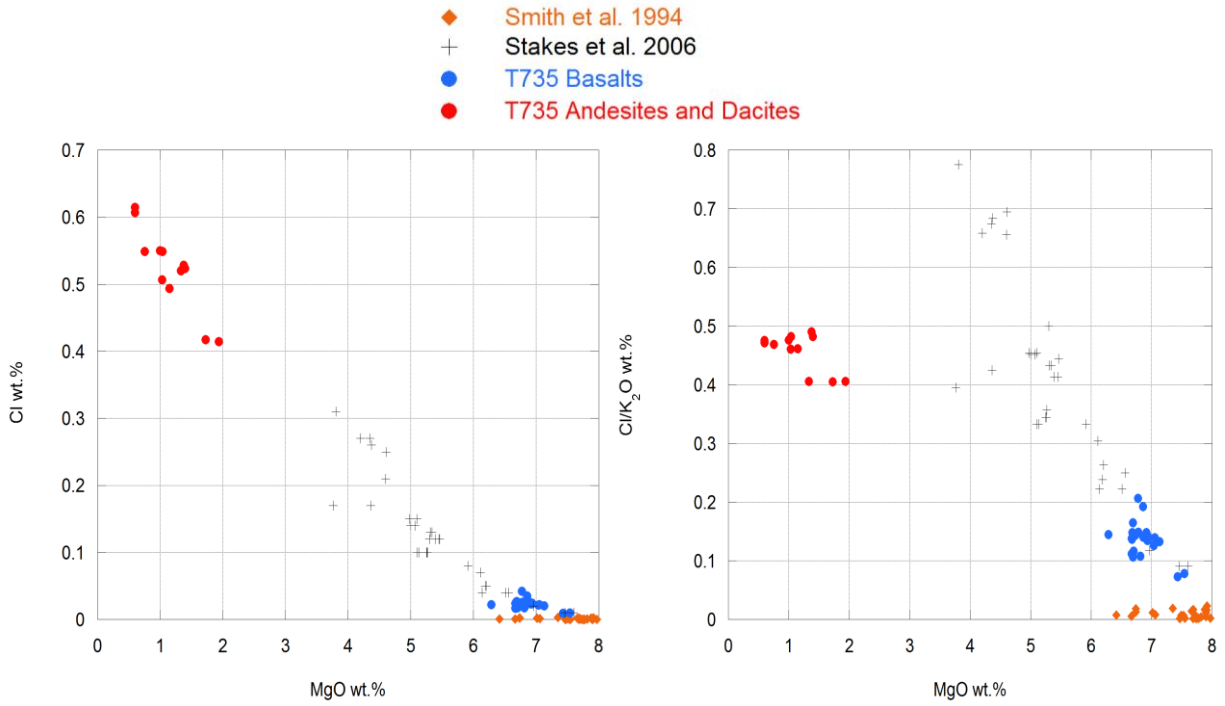


Figure 4-2. Chlorine variations in dive T735 lavas and Cleft segment lavas from Smith et al. 1994 and Stakes et al. 2006. A.) MgO v Cl and B) MgO v Cl/K₂O

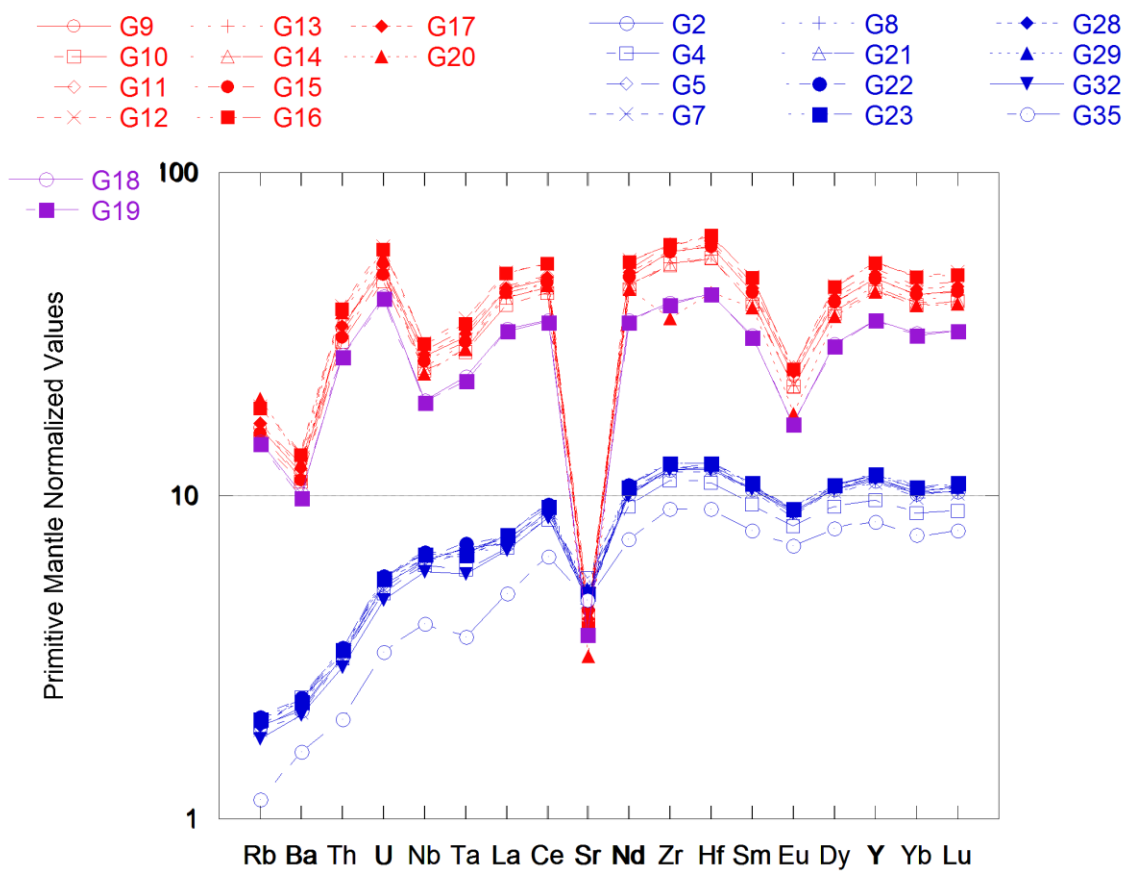


Figure 4-3. Primitive mantle normalized trace element diagram of T735 basalts (blue symbols), andesites (purple symbols) and dacites-rhyodacites (red symbols).

CHAPTER 5 PETROGRAPHY AND MINERAL CHEMISTRY

Basalts

Dive T735 basalts and ferrobasalts are slightly phyric containing < 10% crystals. They contain plagioclase and clinopyroxene phenocrysts (up to 2 mm in size) that are subhedral to euhedral and display subophitic cotectic intergrowth relationships. Smaller microphenocrysts < 1 mm typically have skeletal or swallowtail shapes, indicative of rapid quenching. FeTi oxides are absent as phenocrysts in both the basalts and ferrobasalts collected. Analyses of plagioclase produce An values ranging from 64 to 69. Clinopyroxene compositions are augitic with Mg#s [Atomic Mg/(Mg+Fe²⁺)*100] of ~81. There is no evidence of xenolithic fragments or resorbed crystals in the basaltic lavas.

Andesites and Dacites

The presence of basaltic xenoliths and mingling between dark and light colored glass in the andesitic and dacitic lavas demonstrates that they have clearly been contaminated and possibly mixed. Their history is complex and descriptions of the dacitic lavas (hereby including andesites unless stated otherwise) are only generalized here due to their heterogeneous nature. They are moderately phyric, containing between ~ 10-30% microphenocrysts (<1 mm) and phenocrysts (up to 2 mm). Glass is tan in color but ranges from dark brown to opaque in areas that have undergone significant amounts of devitrification or are in close proximity to basaltic xenoliths. Vesiculation is significant in the dacites, representing up to 15% compared to < 2-3% in the basalts. The vesicles have rounded or elliptical shapes up to several cm in size, which are commonly flow aligned in the direction of the groundmass crystals.

Plagioclase is absent from the groundmass which is dominated by elongated and skeletal pyroxenes (Figure 5-1d). However, larger crystals of pyroxene, plagioclase, FeTi oxides, olivine, quartz, and zircon are present in smaller proportions. Several populations of crystal clots and basaltic xenoliths in the dacites are outlined below on the basis of their mineral assemblage, composition and texture. The term 'basaltic xenolith' is applied only to fragments consisting of large amounts of opaque glass, whereas the term 'crystal clot' refers to clusters of crystals that may have only a thin rim of opaque glass surrounding them. Mineral populations of both individual crystals and those in crystal clots are also characterized here on the basis of their chemical compositions and textures, as described below.

Microphenocrysts and Phenocrysts

Pyroxene

Microphenocrysts and phenocrysts of pyroxene are subdivided into three types on the basis of their core Mg#'s and textural features. Pyroxene compositions range from high-Ca diopside and hedenbergite to low-Ca pigeonite and ferropigeonite (Figure 5-2). A representative list of chemical analyses from core-rim pairs for each population is given in Table 5-1.

Type 1 pyroxenes are normally zoned and are characterized by a Mg-rich clinopyroxene or low-Ca pyroxene core, with Mg#s ranging from 68-80 (Figure 5-3a). They are subhedral to euhedral, less than 1 mm in size, and lack resorption features. A thin (<5 microns) brown rim commonly surrounds colorless cores (Figure 5-1b). The rims are sharp and may be significantly more evolved than the cores, with Mg#s as low as 42 (Figure 5-3a). However, their relatively small size makes it difficult to obtain precise analyses of the rim in many cases.

Type 2 pyroxenes are reversely zoned and are characterized by a Fe-rich clinopyroxene or Fe-rich low-Ca pyroxene core, with Mg#s ranging from 17-54 (Figure 5-3a). The crystals are generally similar in size to type 1 pyroxene, but may be as large as 2 mm. Most type 2 pyroxenes are anhedral and are commonly embayed with resorbed edges. Like type 1 pyroxenes, a sharp brown colored rim often surrounds the original core (Figure 5-1c). Rim compositions span a wide range from Mg#s of 22 – 73, with average Mg#s of ~50 (Figure 5-3a). However, the rims are always less evolved than their core composition. The brown colored rims surrounding type 2 pyroxenes may be wider (up to 20 microns) than those surrounding type 1. Wider reaction rims are sometimes patchy, containing both small amounts of glass and higher Mg# pyroxene. Some type 2 ferroaugites contain exsolved lamellae of low Ca-pyroxene that are <5 microns wide, suggesting that they have had a protracted cooling history.

The third type of pyroxene characterized here occurs in the groundmass and is distinguished by its brown color and smaller grain size (<20 microns in width). It occurs as either euhedral crystals that are < 20 microns in size or as elongated-skeletal grains up to 1mm in length but generally less than 5-10 microns in width (Figure 5-1d). Some of the elongated crystals are more appropriately termed crystallites, exhibiting a needle like morphology, often developing fascicular textures. The cores of type 3 pyroxenes may contain a colorless nuclei (1-5 microns) that is considerably more mafic (Mg#'s up to 76) than the rims, which have average Mg#s of 55 (Figure 5-3a). These rounded nuclei are similar to type 1 pyroxene in both composition and lack of color, suggesting that the nuclei may have originated from a relatively mafic magma. However, distinctions between analyses with colorless nuclei and those without are difficult due to their

smaller grain size and difficulty of distinguishing the two using backscatter electron imaging.

A number of analyses plot within the pyroxene miscibility gap (Figure 5-2). These analyses may be metastable pyroxenes that crystallized rapidly during quenching of the liquid (Mazzullo and Bence, 1976). Alternatively, this may reflect analysis of a combination of both pigeonite and augite, similar to pyroxenes analyzed in andesites from the Galapagos Spreading Center (Perfit et al. 1983). This is clearly the case for type 2 pyroxenes where thin exsolved lamellae of ferropigeonite occur within the ferroaugites. Low-Ca pyroxene has been analyzed in all pyroxene types (Figure 5-3b), however, analyses are rare and petrographic distinctions cannot be made between clinopyroxene and low-Ca pyroxenes in thin sections.

Plagioclase

Plagioclase compositions range from An₂₅₋₇₂ and are separated here into two distinct populations, neither of which appear as a groundmass phase. Although plagioclase spans a wide range of compositions, individual crystals are usually only weakly zoned. Representative plagioclase compositions are provided in Table 5-2.

Type 1 plagioclase is typically less than 0.5 mm in length and euhedral to subhedral with cores that have An# > 60. They generally lack resorption features, similar to type 1 pyroxene. Normal zoning occurs in most crystals, however, reverse zoning may occur in crystals that span smaller ranges of An content (<10%) from core to rim (Figure 5-4).

Type 2 plagioclases are generally larger than type 1 (up to 2 mm), anhedral, and have core compositions with An# < 53. They are reversely zoned, although they may show normal zoning if the core and rim vary by only small amounts of An content

(Figure 5-4). Type 2 plagioclase is commonly resorbed and may contain melt inclusions that are similar in composition to the host glass.

FeTi Oxides

Most FeTi oxides analyzed are titanomagnetites with ilmenite being extremely rare and often too small to precisely analyze. A single titanomagnetite-ilmenite pair has been analyzed from sample T735-G12 (the T735 dive number is removed from all preceding sample names) yielding temperatures of ~800-875°C (Schmitt et al. 2011). The titanomagnetites analyzed are composed of 19-24 TiO₂ wt.% and 68-75 FeO^T wt.%. Some oxides appear to be embayed while others display skeletal textures. Individual populations could not be discerned on the basis of texture and chemical composition from the collected analyses.

Olivine

Olivine is rare in the dacites. It is generally < 1 mm in size, yellowish-green, anhedral, and is commonly highly resorbed. It is fayalitic in composition ranging from Fo₇-Fo₂₇ with most analyses below Fo₁₅ (Figure 5-2). Zoning is not significant in olivine, although a thin reaction rim (Fo₂₇) mantles a Fo₇ core in one instance.

Accessory Phases

Quartz crystals up to 0.5 mm in size are present in thin section G20, which is one of the highest SiO₂ (65.75 wt.%) glasses analyzed. They are rounded, highly resorbed, embayed and typically contain melt inclusions that are similar in composition to the dacitic lavas. Myrmekitic intergrowths occur in thin sections G19 and G20. These intergrowths occur as mm sized resorbed fragments. Small (<100 micron) euhedral or skeletal zircons are also present in the dacites. They are sometimes embayed and overgrown by euhedral rims (Schmitt et al., 2011). The zircons were previously

analyzed by Schmitt et al. (2011), who obtained a U-Th crystallization age of 29.3 ± 4.8 ka and crystallization temperatures of $905 \pm 34^\circ\text{C}$ using Ti-in-zircon thermometry.

Crystal Clots

Four types of crystal clots are identified here, each of which is classified on the basis of their mineral assemblage, chemistry and texture. Type A clots are composed of T1 pyroxene + T1 plagioclase +/- FeTi oxides that appear to be a late crystallizing phase. Individual clots are generally less than 1 mm and are irregularly shaped. A quenched rim of dark glass sometimes surrounds the clot of crystals. Unlike the individual microphenocrysts of T1 pyroxene and plagioclase, these crystals are typically skeletal and commonly demonstrate subophitic intergrowth textures (Figure 5-1a).

Type B clots include T2 pyroxene + T2 plagioclase +/- FeTi oxides (Figure 5-1c). They are generally larger than type A clots, up to a few mm in size. Unlike type A clots, textural features such as morphology and size cannot be used to distinguish individual microphenocrysts of T2 plagioclase and pyroxene from those in clots.

Type C clots are defined by T2 plagioclase and fayalitic olivine. Type 2 plagioclase compositions (An_{30-35}) are more restricted than those found in type B clots. A single clot (type D) of skeletal olivine (Fo_{80}), plagioclase (An_{66}) and clinopyroxene with Mg# of 77 is found in sample G20. The clot is ~ 2 mm in size with individual crystals up to 0.5 mm in length. The skeletal olivine's core (Fo_{80}) is rimmed by Fo_{49} , indicating it equilibrated in or reacted with a significantly more evolved liquid after initial crystallization.

Basaltic Xenoliths

Basaltic xenoliths are made up of plagioclase + augite +/- pigeonite +/- FeTi oxides + basaltic glass. They are easily distinguished from crystal clots by the significant amounts of opaque glass that surround the groundmass and phenocrysts (Figure 5-5a).

Plagioclase (An_{64-72}) and pyroxene (Mg# 71-82) are compositionally similar to T1 pyroxene and T1 plagioclase (Table 5-2). Two types of basaltic xenolith are distinguished here on the basis of morphology and crystallinity.

The first type is characterized by its rounded to subrounded morphology. It ranges from holohyaline to hypocrySTALLINE with a quenched glassy rind surrounding each xenolith. In some cases the rounded basaltic xenoliths are intruded by lighter colored dacitic glass (Figure 5-5d). Grain size generally coarsens towards the center of the xenoliths. Subophitic crystal clots similar in mineralogy, size and shape to type A clots may be located in the xenoliths interior (Figure 5-5b). The second type of basaltic xenolith distinguished here is characterized by its angular or jagged morphology (Figure 5-5c). It is usually larger, up to several centimeters in size, is generally aphyric and does not typically have a glassy rind surrounding its rim.

Table 5-1. Representative Pyroxene Analyses

Sample	735-9-CPX3-1	735-9-CPX3-4	735-14-Pyx12	735-14-Pyx12	735-11-Pyx1
Type	T1	T1	T2	T2	T3
Location	Core	Rim	Core	Rim	Core
Mg#	80.2	61.92	23.81	53.55	57.57
SiO ₂	50.72	50.46	48.5	50.74	48.64
TiO ₂	1.08	0.95	0.21	0.65	1.57
Al ₂ O ₃	3.39	1.99	0.26	1.56	3.28
FeOt	9.01	15.38	38.21	21.63	16.45
MnO	0.2	0.41	0.98	0.61	0.4
MgO	16.46	13.38	6.7	13.99	11.95
CaO	18.45	16.53	4.25	9.53	16.2
Na ₂ O	0.26	0.27	0.04	0.15	0.33
K ₂ O	0	0	0	0.01	0.01
P ₂ O ₅	0.01	0.08	0.03	0	0.07
Cr ₂ O ₃	0.2	0.07	0	0.01	0
NiO	-	-	0.03	0	0
Total	99.77	99.52	99.21	98.89	98.89
Sample	735-11-Pyx1	735-9-Pyx2	735-9-Pyx2	735-19-xeno	735-19-xeno
Type	T3	T3	T3	BX	BX
Location	Rim	Core	Rim	Core	Rim
Mg#	51.97	61.17	53.22	80.78	71.16
SiO ₂	49.38	47.54	49.33	53.85	46.83
TiO ₂	0.91	2.18	0.98	0.56	2.51
Al ₂ O ₃	1.55	3.96	1.89	1.84	7.67
FeOt	20	15.4	18.5	7.32	11.05
MnO	0.53	0.38	0.48	0.21	0.21
MgO	11.84	12.76	11.19	17.26	13.92
CaO	13.88	15.6	16.17	18.11	16.56
Na ₂ O	0.19	0.32	0.27	0.26	0.4
K ₂ O	0.02	0	0.02	0.01	0.03
P ₂ O ₅	0	0.1	0.05	-	-
Cr ₂ O ₃	0.01	0	0.02	-	-
NiO	0.01	0	0.02	-	-
Total	98.32	98.24	98.9	99.42	99.17

Table 5-2. Representative Plagioclase Analyses

Sample	735-20- Plag1	735-20- Plag1	735-9- Plag10	735-9- Plag10
Type	T1	T1	T2	T2
Location	Core	Rim	Rim	Core
An#	68.86	70	46.49	43.39
SiO ₂	50.86	50.02	55.93	57.54
TiO ₂	0.05	0.05	0.03	0.04
Al ₂ O ₃	30.26	29.92	26.32	26.49
FeOt	0.52	0.58	0.49	0.38
MnO	0.01	0.02	0.01	-
MgO	0.19	0.23	0.04	0.04
CaO	14	14.15	9.49	9.11
Na ₂ O	3.47	3.31	5.95	6.47
K ₂ O	0.05	0.06	0.14	0.15
P ₂ O ₅	-	0.01	-	0.02
Cr ₂ O ₃	-	-	0.01	0.01
NiO	0.04	0.01	0.01	0
Total	99.45	98.37	98.42	100.24
Sample	735-20- Plag8	735-20- Plag8	735-20- PI3BX	735-20- PI3BX
Type	T2	T2	BX	BX
Location	Core	Rim	Core	Rim
An#	31.39	28.88	69.75	66.47
SiO ₂	60.56	60.98	50.84	51.47
TiO ₂	-	-	0.06	0.1
Al ₂ O ₃	24.5	23.82	30.33	29.7
FeOt	0.33	0.33	0.66	0.84
MnO	0	0.02	0.01	0.01
MgO	0.02	-	0.2	0.22
CaO	6.5	6.01	14.23	13.48
Na ₂ O	7.7	8.02	3.4	3.72
K ₂ O	0.22	0.25	0.02	0.05
P ₂ O ₅	-	-	0.03	0.03
Cr ₂ O ₃	-	-	0.01	-
NiO	-	-	0.02	0.01
Total	99.82	99.43	99.81	99.65

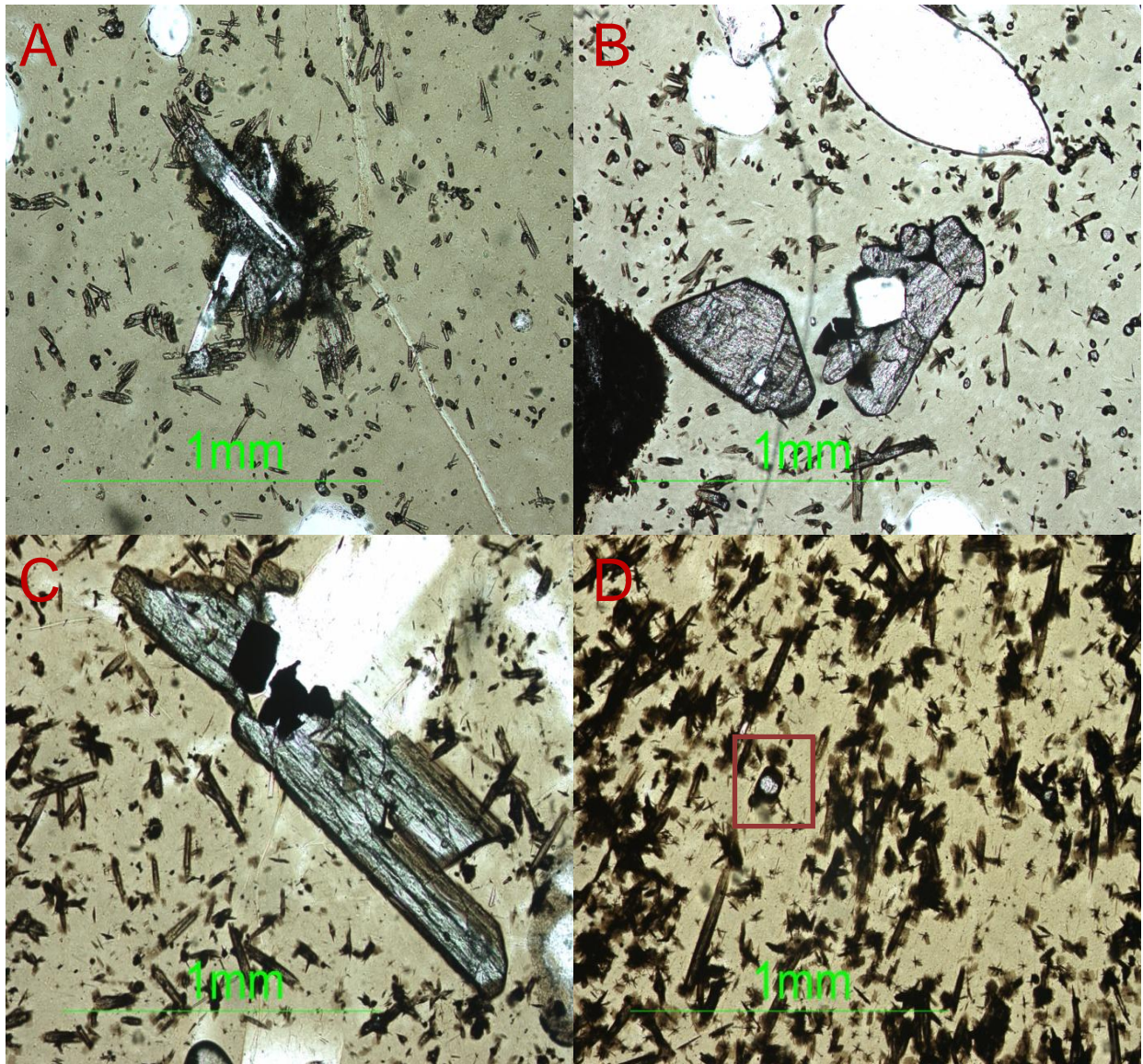


Figure 5-1. Plane polarized light images of characterized pyroxene types A) Image of type A crystal clot with T1 pyroxene + T1 plagioclase, note the elongated fibers of pyroxene that have crystallized on plagioclase B) Image of type A crystal clot with subhedral T1 pyroxene + T1 plagioclase + FeTi oxides. Large white (clear) oblong features are vesicles C) Image of T2 pyroxene with brown rim + T2 plagioclase + FeTi oxides in type B clot D) Image of type 3 pyroxenes, the red box indicates the rounded colorless nuclei discussed in text.

A

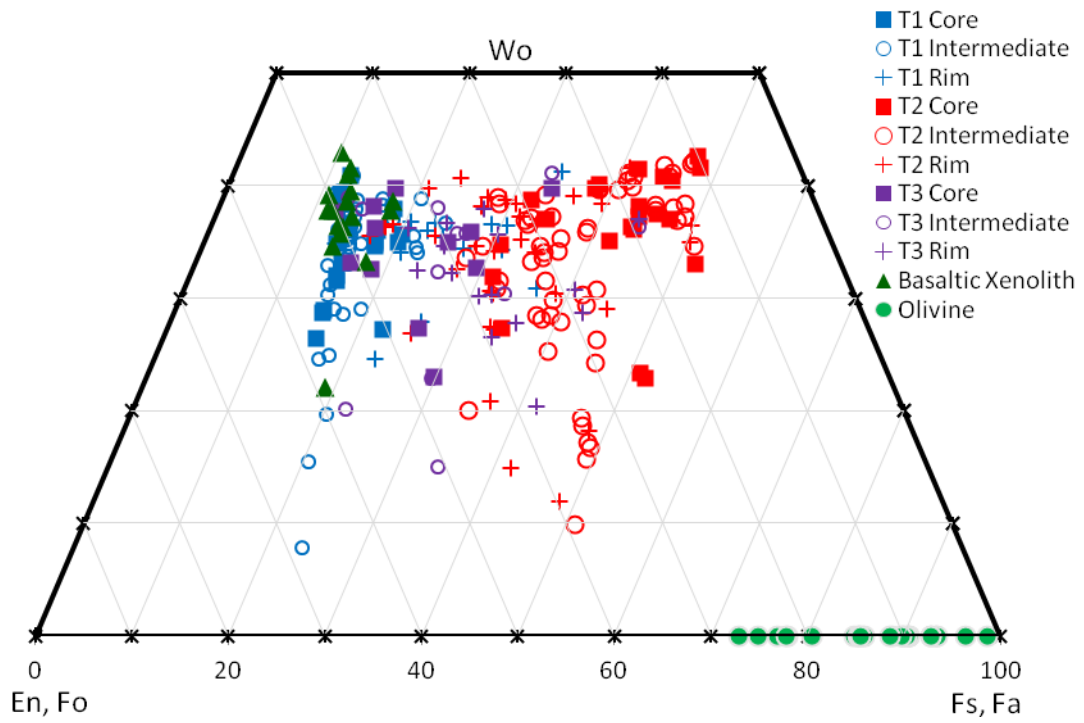
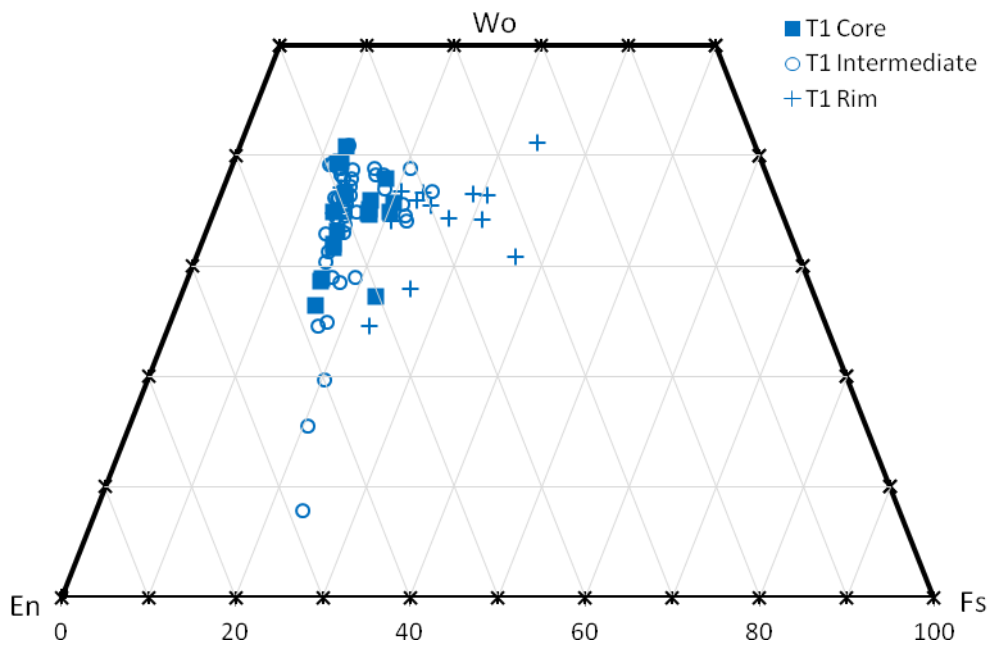


Figure 5-2. Pyroxene and olivine compositions in T735 andesites and dacites A) All data B) Type 1 pyroxene C) Type 2 pyroxene D) Type 3 pyroxene.

B



C

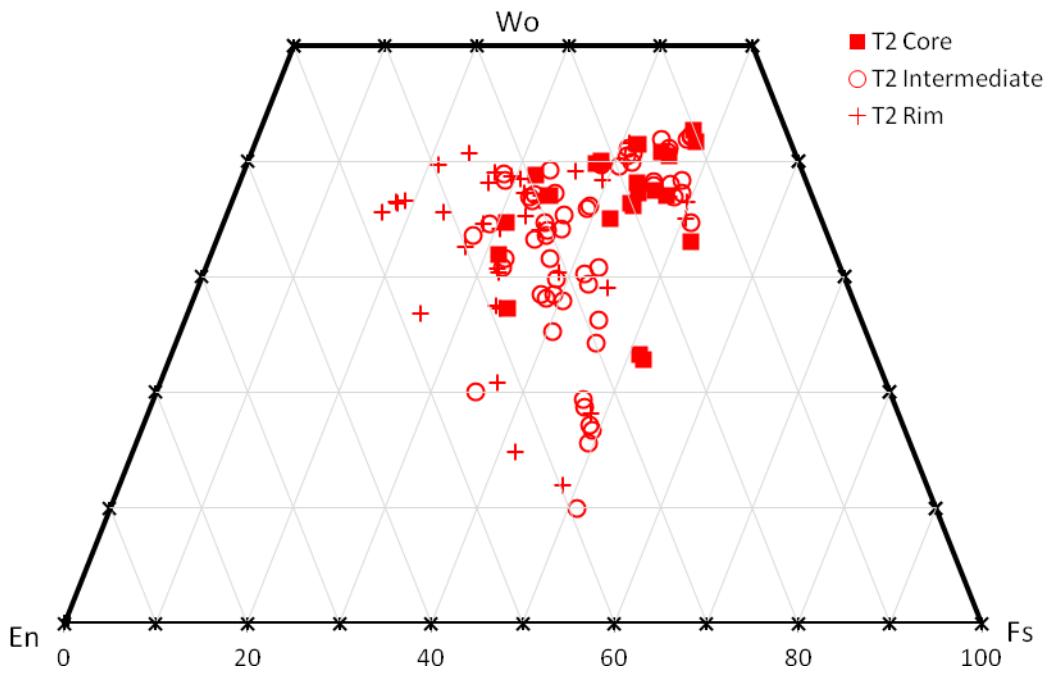


Figure 5-2. Continued

D

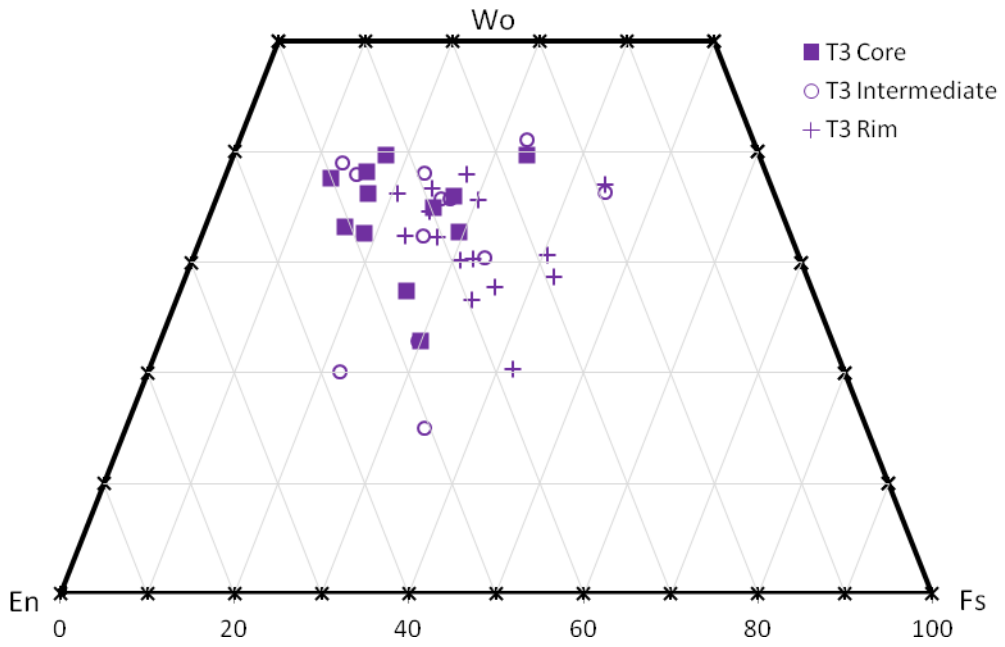


Figure 5-2. Continued

- T1 Core
- T1 Rim
- T2 Core
- T2 Rim
- T3 Core
- T3 Rim

A

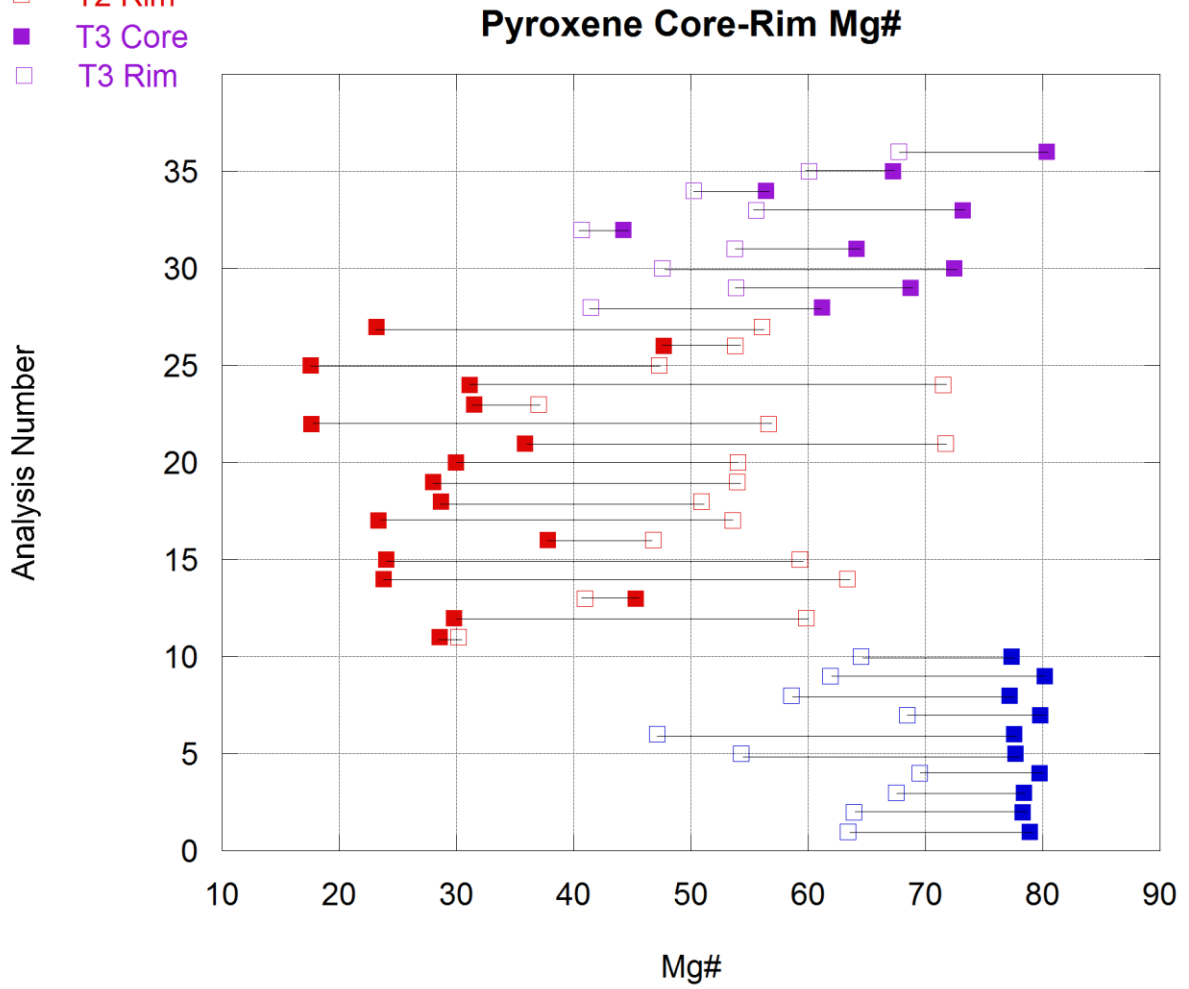


Figure 5-3. Pyroxene core to rim chemical variations in A) Mg# and B) CaO for type 1, 2 and 3 pyroxenes. Open squares indicate rims and closed squares are cores

- T1 Core
- T1 Rim
- T2 Core
- T2 Rim
- T3 Core
- T3 Rim

B

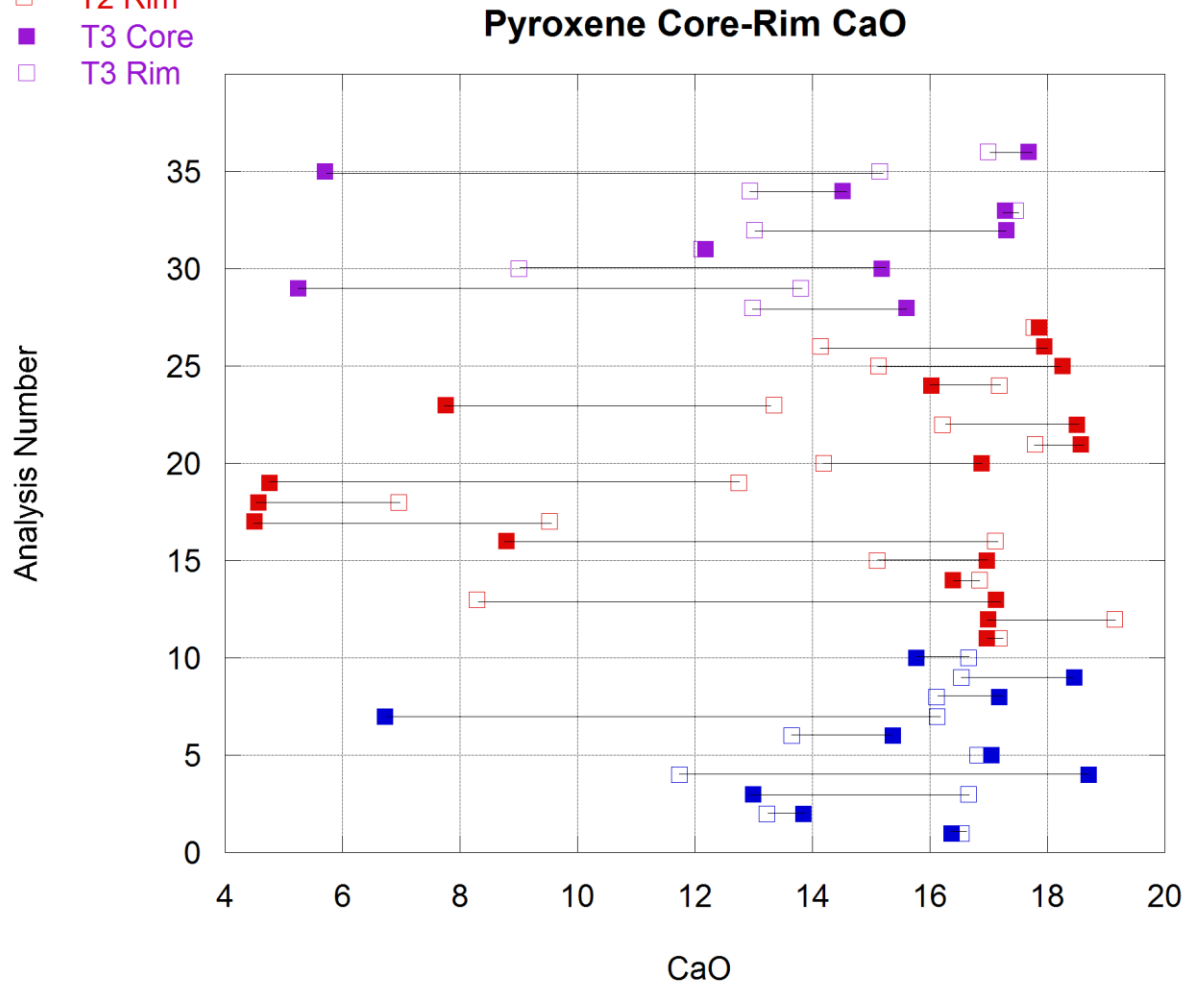


Figure 5-3. Continued

- T1 Core
- T1 Rim
- T2 Core
- T2 Rim

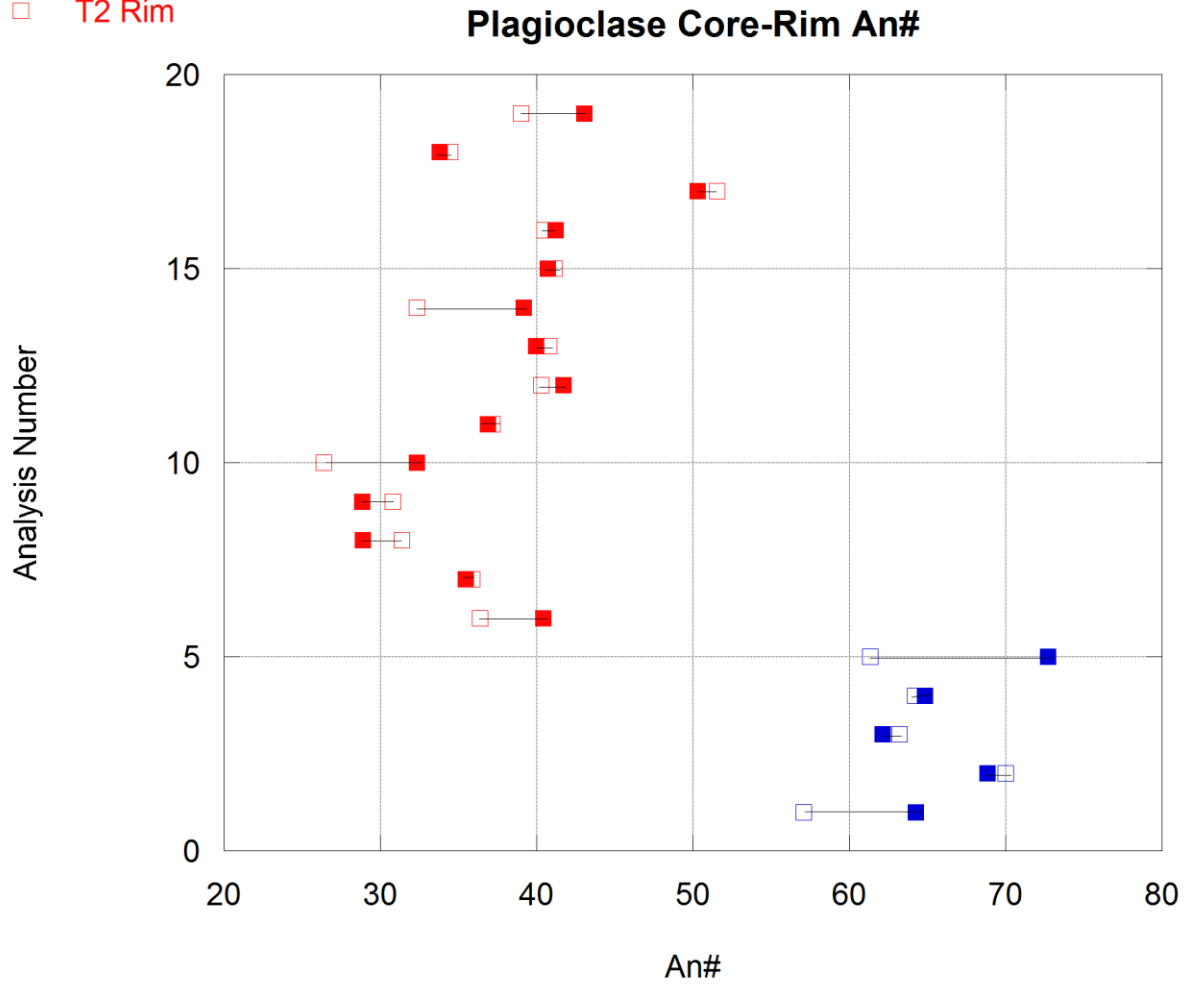


Figure 5-4. Plagioclase core to rim An# variations for individual crystals of type 1 and 2 plagioclases. Open squares indicate rims and closed squares are cores.

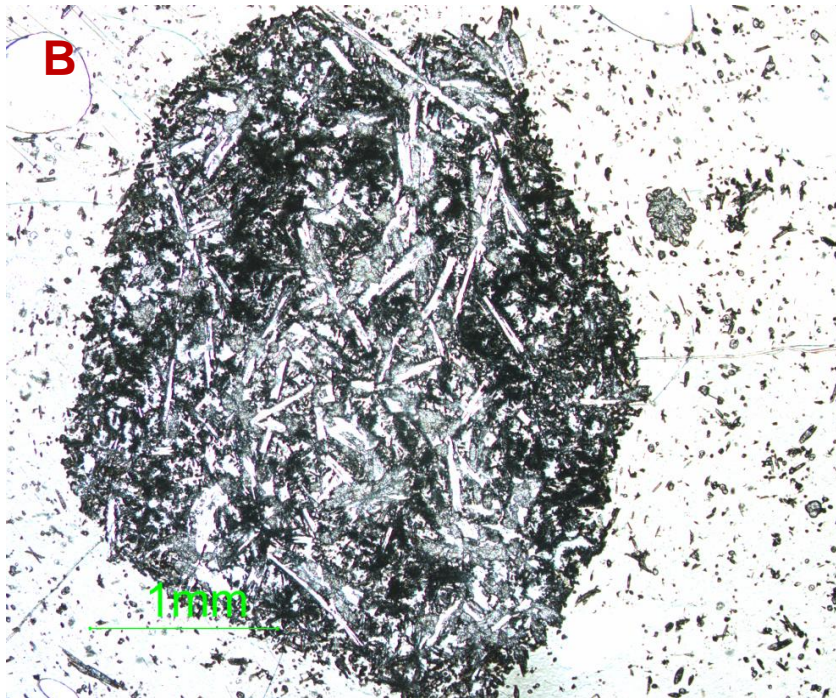
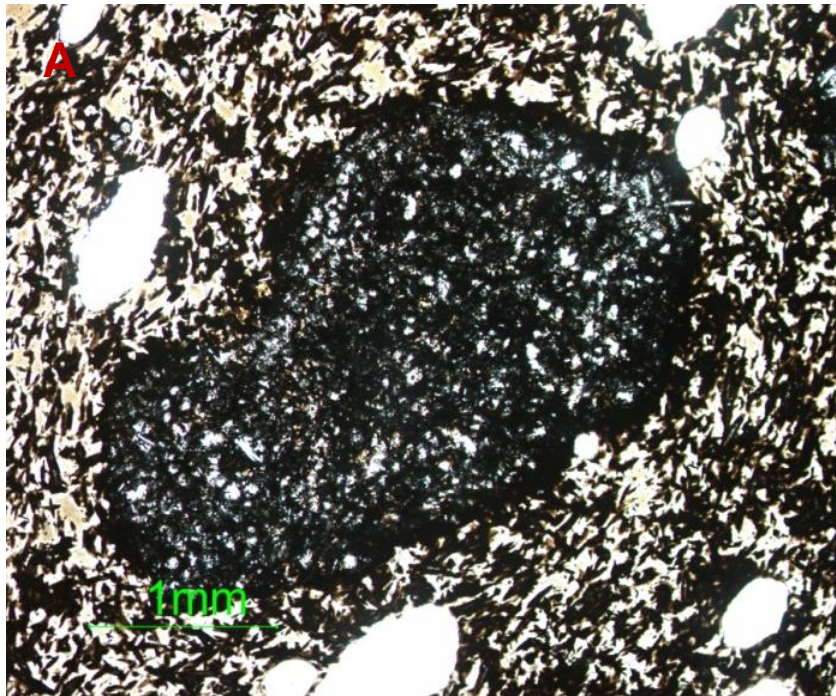


Figure 5-5. Plane polarized light images of basaltic xenoliths. A) Type 1 rounded basaltic xenolith with chilled margins B) Type 1 basaltic xenolith with coarser crystals in its interior and C) Type 2 basaltic xenolith with a more angular morphology and jagged margins. D) Image of type 1 basaltic xenolith being intruded by dacitic glass.

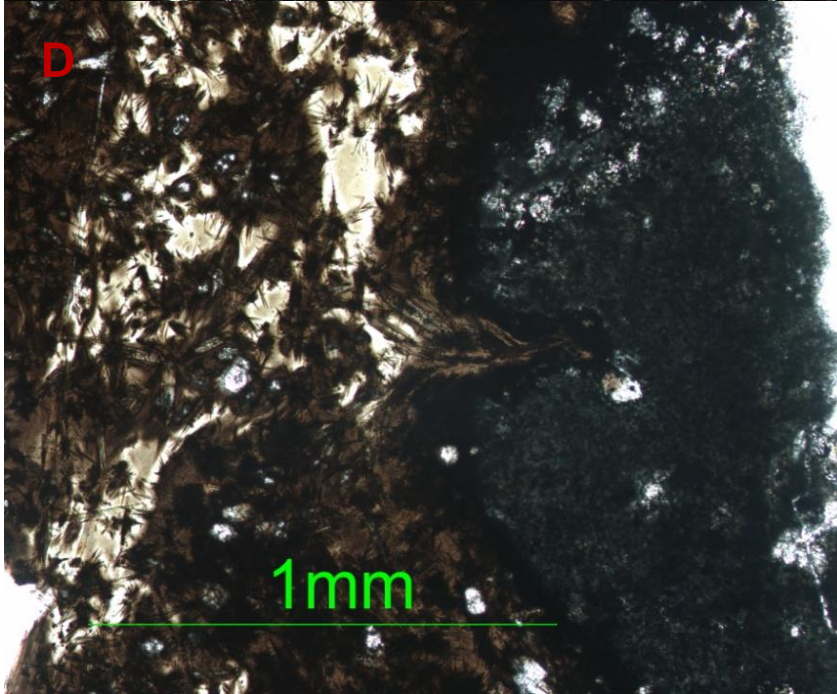
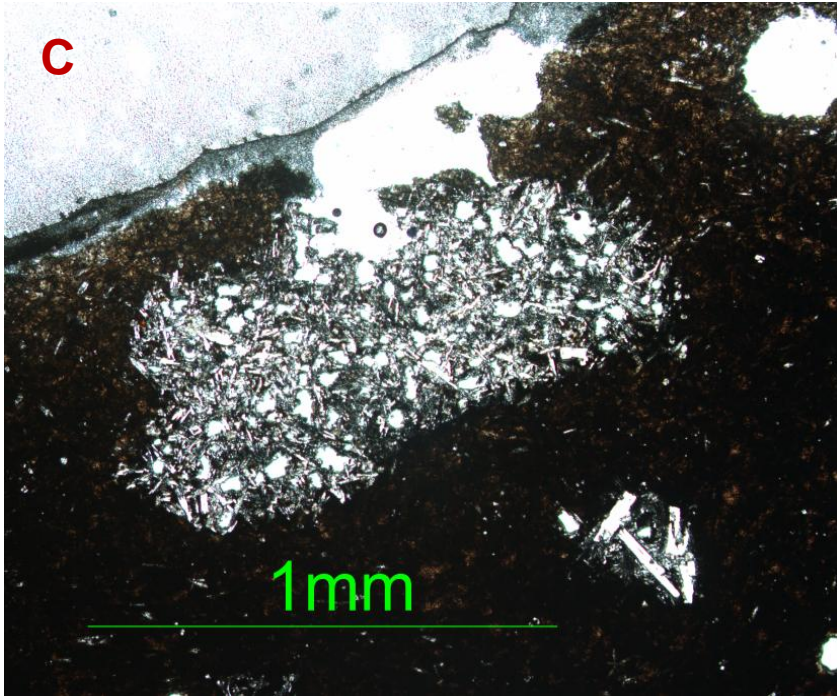


Figure 5-5. Continued

CHAPTER 7 DISCUSSION

Fractional Crystallization

Extensive sampling of MOR lavas from RAD's at 85°W GSC, 9° N EPR, and the southern JdFR have yielded lavas ranging from relatively primitive basalt to rhyodacite that follow typical tholeiitic differentiation trends (Perfit et al. 1983; White et al. 2009; Wanless et al. 2010) (Figure 7-1). As discussed by Wanless et al. (2010) the major and trace element compositions of these suites are remarkably similar. Although there is a compositional gap in JdFR data from ~ 2 to 4 MgO wt.%, there is evidence suggesting that some of the southern JdFR lavas may be products of extreme crystal fractionation as has been concluded for other MOR dacitic suites. For example, high amounts (~ 75-85%) of crystal fractionation have been proposed to explain the occurrence of high silica andesites from the 85°W GSC along with minor amounts of mixing (Perfit and Fornari, 1983; Perfit et al. 1983, Juster et al. 1989). Furthermore, pyroxenes from the southern JdFR dacites produce trends similar to large igneous intrusions like Bushveld and Skaergaard complexes, that increase in Fe content as fractional crystallization proceeds (Taylor, 1964; Atkins 1969; Nwe 1975) (Figure 7-2). In particular, low-Ca pigeonite is absent beyond Fs_{65} similar to both the Skaergaard and Bushveld suites (Figure 7-2). However, fractional crystallization has been extensively modeled by Wanless et al. (2010) who show that although ~75-85% crystallization of a ferrobasaltic parent can produce most major element trends, it does not produce all of the chemical variations found in the dacitic lavas. In particular values of K_2O , Al_2O_3 and Cl are higher and P_2O_5 lower in the dacitic magmas than the predicted values (Wanless et al. 2010). Furthermore, incompatible trace elements require even greater degrees (>90%) of

fractional crystallization, suggesting that other processes must be taking place.

Petrographic evidence indicates that magma mixing may play a role, which is evaluated below.

Evidence Supporting Magma Mixing

Several petrographic features in the dacitic lavas suggest that magma mixing may have played an important role in their evolution. These features include (a) the presence of basaltic xenoliths, mafic clots and mafic xenocrysts, (b) resorbed mineral phases that are in disequilibrium with their host glass, (c) olivine reaction rims (Fe_{80} to Fe_{49}) in type D clots and (d) complexly zoned pyroxenes with rim values that approach intermediate compositions between the two end members.

Two types of basaltic xenoliths and two mafic crystal clots (types A and D) were incorporated into the dacitic lavas. Type 1 xenoliths, exhibit rounded morphologies, chilled margins and decreasing grain size from the center of the xenolith to the rim, which indicate that they were liquid prior to being incorporated into the dacites. The irregular shapes, jagged edges, and lack of a chilled margin in type 2 basaltic xenoliths indicate that they may instead be pieces of wall rock that have been mechanically transferred and partially assimilated into the dacitic magma. Type A crystal clots are similar in both mineralogy and texture (e.g. acicular pyroxene, swallow tail plagioclase) to the coarser crystals located at the cores of some type 1 basaltic xenoliths. It is likely that type A clots originated from the same source as the type 1 basaltic xenoliths based on their similar chemistry and textural features. The presence of skeletal olivine in type D crystal clots suggests that more than one magma type was involved in mixing with sample G20.

The more evolved mineral phases (e.g. iron-rich T2 pyroxene, sodic T2 plagioclase, fayalitic olivine, FeTi oxides and quartz) commonly display resorbed margins. The effect of assimilating lower temperature, more evolved mineral phases into high temperature (less evolved) magmas was first described by Bowen (1928). Lower temperature phases will react by dissolving in higher temperature magma. If the mineral phase is saturated within a magma a reaction rim may develop and the new rim will be compositionally equivalent to that which is in equilibrium with the magma (Bowen 1928). Type-two (T2) pyroxenes demonstrate this phenomenon, their corroded cores typically are surrounded by a reaction rim that is less evolved (higher Mg#) and occasionally has a sieve like texture within the core. Resorption may also occur due to changes in pressure. Plagioclase, for example, will become unstable if it undergoes decompression and has a more sodic composition than that which is stable in the melt (Pearce et al. 1987). Although decompression may account for resorption of plagioclase it does not easily explain resorption features in other mineral phases like pyroxene, olivine, or quartz whose stabilities are less sensitive to small changes in pressure.

Higher temperature xenocrysts do not dissolve in lower temperature melts (Bowen, 1928). Instead they will continue to grow if the phase is saturated in the melt, rimmed by the composition which is in equilibrium with the melt (Bowen 1928, Shelley 1983). This is consistent with T1 pyroxenes, which lack resorption features and are typically rimmed by more Fe-rich compositions. Unlike T1 pyroxene, T1 plagioclase does not appear to have a reaction rim. However, plagioclase does not appear to be a stable phase in the dacitic lavas because it does not appear as a microphenocryst or

phenocryst of the groundmass. Recent experimental studies on dacitic lavas collected from the Pacific-Antarctic Ridge, with similar compositions to dacites in this study, show that plagioclase crystallizes after clinopyroxene in a water saturated system and temperatures $< 1000^{\circ}\text{C}$ (Koepke personal communication). Alternative explanations may include mixing driving plagioclase off the liquidus, suppression of plagioclase due to high H_2O or possibly rapid quenching prohibiting nucleation of plagioclase in the more viscous dacites. However, the lack of zoning in plagioclase relative to the pyroxenes suggests that kinetics has not played a major role and that plagioclase is instead not saturated in the melt.

The documented compositional variations in pyroxene provide a compelling argument in support of magma mixing. The cores of T1 and T2 pyroxenes appear to be bimodal, with average Mg#s of 75 and 33, respectively. However, the rims of T1 and T2 pyroxenes converge with those of intermediate composition T3 pyroxenes at Mg# ~ 55 , consistent with being in equilibrium with several of the dacitic glasses (Figure 7-3b). T2 pyroxenes crystallized from a melt more evolved than that of the dacites. The phase chemical data (Figure 7-3a) also indicate that T3 cores are more magnesian than their rim compositions, similar to those of T1 pyroxenes. The colorless nuclei of many T3 cores and their relatively magnesian compositions indicate that some T3 cores originally crystallized in basaltic magmas.

Mineral-Melt Equilibrium

The petrographic and chemical arguments supporting magma mixing discussed above favor the interpretation that many of the mineral phases are xenocrysts. The minerals that display resorption features (T2 pyroxene, T2 plagioclase, fayalitic olivine, FeTi oxides and quartz) likely crystallized in a magma even more evolved than the

dacitic host glass. An attempt to constrain the composition of that end member magma is made here using mineral-melt equilibria.

The Mg# of melts which are in equilibrium with the cores and rims of T1, T2, and T3 pyroxenes can be constrained using mineral-melt equilibria. The $^{Fe/Mg} K_D$ values for clinopyroxene-liquid are relatively constant in basalts and andesites, with average values of 0.27 ± 0.03 (Grove and Juster, 1989; Kinzler and Grove, 1992). These values are less well constrained for high silica dacites and rhyolites, however, this value is believed to increase to > 0.35 in magmas with > 5 wt % H₂O (Gardner et al. 1995; Grove et al. 2003; Frey and Lange 2011). Although the dacitic magmas are relatively hydrous for MOR lavas, they are generally < 2 wt% H₂O, thus typical $^{Fe/Mg} K_D$ values of 0.27 ± 0.03 for clinopyroxene-liquid equilibria are used here (Figure 7-4). Pyroxene cores and rims that lie within the error envelope in Figure 7-4 are considered to be in equilibrium, while those that lie outside are in disequilibrium with their host glass.

The cores of the most primitive T1 pyroxenes (Mg# ~ 80) and several of the pyroxenes from basaltic xenoliths are in equilibrium with melt with Mg#'s of ~ 55 or as low as 47 using a Kd value of 0.24 and as high as 58 using a Kd value of 0.30 (Figure 7-4). This is consistent with the ferrobasalts collected from dive T735 which have a mean Mg# of 52.5. Most of the pyroxene rim compositions lie within the equilibrium boundaries of the andesitic and dacitic glasses, which have Mg#'s ranging from 30.2 to 13.1. T2 pyroxene cores that lie below the equilibrium boundaries are in equilibrium with melt Mg#'s ranging from ~ 6 to 14. Only samples G12 and G16, which are the most evolved lavas collected fall within this range and have Mg#'s of 12.9 and 13.1,

respectively. While the most evolved T735 lavas collected may be in equilibrium with some T2 cores, a more evolved melt is required to explain the lower Mg# cores.

Fayalitic olivine xenocryst compositions can be used to further assess the range of equilibrium melt compositions required for the evolved mineral phases. The Fe/Mg K_D between olivine and liquid has a constant value of 0.30 ± 0.03 that is independent of changes in composition and temperature (Roeder and Emslie, 1970; Ussler III and Glazer, 1989). Fayalitic olivine Mg#s ranging from ~2 to 29 are in equilibrium with melt Mg#s of ~ 1 to 11, spanning the entire range of K_D values from 0.27 to 0.33 (Figure 7-5). This is consistent with the predictions of a more evolved end member, as illustrated by clinopyroxene-liquid equilibria calculations. However, the olivine compositions require an even more evolved end member (possibly as low as Mg# ~ 1) and are too Fe-rich and or Mg-poor to be in equilibrium with any of the dacitic glasses. This supports the high amounts of resorption and general scarcity of fayalitic olivine. Furthermore, it is only found in lavas with more than 63 wt.% SiO₂ and Mg# < 17.9 .

Magma Mixing

Although physical and mineralogic evidence indicate magma mixing clearly played a role in the development of the andesites and dacites, the extent to which mixing is responsible for their chemical variability and whether they can be related through mixing of only two end members has not yet been established. Differences in sources, degrees of partial melting of these sources and/or extents of fractionation can produce a wide range of evolved end member compositions, leading to an array of possible mixing lines. Furthermore, the extent of fractional crystallization of the mafic end member may also lead to an array of potential mixing lines. This appears to be true for several basaltic andesites from Stakes et al. (2006), which diverge from the main LLD between

~ 6 to 4 MgO wt.%. Because dacitic glasses and their whole rock equivalents follow fairly linear chemical trends and their trace element abundance patterns are very similar (Figure 7-6), it is likely that heterogeneities and varying degrees of partial melting play only a minor role in their development and that the evolved end member melts had a narrow range of compositions.

The presence of fayalitic olivine in equilibrium with glass Mg#'s of ~1 to 11 indicates they must have originated from a lower Mg# melt than the most evolved rhyodacite collected from dive T735 (G12) with Mg# of 13. Since the composition of sample G12 is known and because it generally follows the main linear trend produced by the dacitic lavas in most variation diagrams, (Figure 7-6) it is used here as the evolved end member composition. If the dacitic lavas can be related through mixing, the most evolved end member (Mg# ~ 1) can be constrained by extending mixing lines to lower MgO and FeO(t) values that approach Mg# of ~ 1.

Basaltic compositions ranging from 3.76 to 7.55 MgO wt.% are evaluated here to constrain the mafic end member compositions involved in mixing. Basalts surrounding the dacitic constructional mounds are an obvious choice for the potential mafic end members, their pyroxene Mg#'s (~ 81) and plagioclase An#'s (64-69) are similar to those found in the basaltic xenoliths (Mg# = 71-82 and An# = 64-72). The most mafic (G35), evolved (G32) and an intermediate (G7) ferrobasalt sample from dive T735 were chosen for mixing considerations, ranging from 6.29 to 7.55 MgO wt.%. The three mixing lines separate the evolved T735 lavas into three distinct groups (a) the main group of dacites which require mixing with a more evolved composition (b) the two andesites G18 & G19, whose trends are conflicting on variation diagrams (i.e. do not fall

on the same mixing lines in multiple plots) and (c) G20 which requires mixing with a more primitive magma (Figure 7-6). Sample G20 is the only sample containing type D clots that include skeletal olivine (Fo80), plagioclase (An66) and clinopyroxene (Mg# = 77), supporting interaction with a more primitive magma than the T735 basalts. Because the two andesites (G19 & G20) do not follow the main linear trend and mixing lines require conflicting mafic end member compositions (depending on the variation diagram used), it is unlikely that the two andesites were produced along mixing lines through sample G12.

In order to successfully model mixing between sample G12 and basaltic magmas to produce the linear trend of the dacites, the mafic end member composition must be more evolved than those collected from dive T735. Therefore, samples T460-G24, T736-G29 and T736-G11 from other areas in the southern Cleft segment are also considered as possible end member compositions. Dives T460 and T736 are north of dive T735 but are still located within the southernmost portion of the Cleft segment. Samples T460-G24, T736-G29 and T736-G11 were collected from the Crestal Boundary Ridge described by Stakes et al. (2006). Their MgO values range from 3.76 to 5.30 wt.% with the most evolved sample (T736-G11) being a basaltic andesite. Mixing lines become increasingly more successful at intersecting the dacitic compositions as the degree of evolution in the basaltic lavas increases, with FeTi basalts and basaltic andesites providing the best fit (Figure 7-6). This is true in all cases except for Al_2O_3 (Figure 7-7) which cannot successfully be modeled by two component mixing of any possible Cleft end member composition.

High Al_2O_3 values in MOR dacites have previously been attributed to the preferential assimilation of amphibole, which can be found in hydrated oceanic crust (Wanless et al. 2010). This is supported by high $\text{Cl}/\text{K}_2\text{O}$ and H_2O values in the dacitic lavas that also cannot be explained by fractional crystallization alone. Dissolution of amphibole during mixing cannot be ruled out, however, amphibole has not been observed in any of the MOR dacites. An alternative hypothesis is that the high Al_2O_3 values are related to crystallization of pyroxene in the mixed dacitic melts. Whole rock compositions have lower Al_2O_3 values than their glasses and they lie below the proposed mixing lines. Because basaltic xenoliths will either increase the Al_2O_3 further or decrease them by only minor amounts it is unlikely that they are responsible for the lower Al_2O_3 values of the whole rocks. However, Al_2O_3 -poor xenocrysts or the abundant pyroxene in the groundmass may play a role. The influence of xenocrysts should be small compared to T3 pyroxene, which may account for up to 20% of some thin sections. Mass balance calculations suggest that Al_2O_3 , MgO and FeO(t) variation between glass and whole rock samples can be attributed to ~ 5 to 7% crystallization of T3 pyroxene (see vectors in Figures 7-6 and 7-7). Although several thin sections contain > 7% pyroxene, this number may be influenced by (a) the wide range of crystallinity (b) minor influence of xenocrysts and (c) the presence of basaltic xenoliths. Therefore, it is difficult to quantify the amount of pyroxene crystallization necessary for the increased values but pyroxene crystallization is consistent with observed differences between the whole rock and glass compositions.

Petrogenesis

Wanless et al. (2010) hypothesize that extreme crystal fractionation of MORB and partial melting and assimilation of altered basaltic or gabbroic crust is responsible for

the development of MOR dacites. An alternative model is proposed here that accounts for both the highly evolved mineral phases in the JdFR dacites and evidence supporting magma mixing. Plagiogranite is the most likely source of the highly evolved phases, supported by the presence of myrmekite and exsolved pyroxene that are produced only by slow cooling. Intrusion of basaltic magma would supply enough heat to cause partial melting of plagiogranite, forming a rhyolitic melt. This rhyolitic melt may then mix (10-40%) with the highly fractionated FeTi basalt or basaltic andesites to produce dacitic magma. The similarity between pyroxene and plagioclase from type 1 basaltic xenoliths and those found in ferrobasalts indicates that a second injection of ferrobasaltic magma remobilized the dacitic magmas but did not extensively mix with them. This is also supported by mingling between light and dark glasses in many instances (Figure 5-5d). High Cl/K₂O in MOR dacites has been attributed to melting of hydrothermally altered crust or mixing with brines (Wanless et al. 2010, 2011). Wanless et al. (2011) favor hydrothermally altered crust over assimilation of saline brines because it supports the major and trace element compositions of the dacitic lavas. However, partial melting of a plagiogranite source could also explain the trace element enrichments and crystallization of pyroxene may explain the high Al₂O₃ wt.%. Therefore, either a hydrothermally altered plagiogranite source or contamination of saline brines may attribute to the high Cl/K₂O in the dacitic lavas.

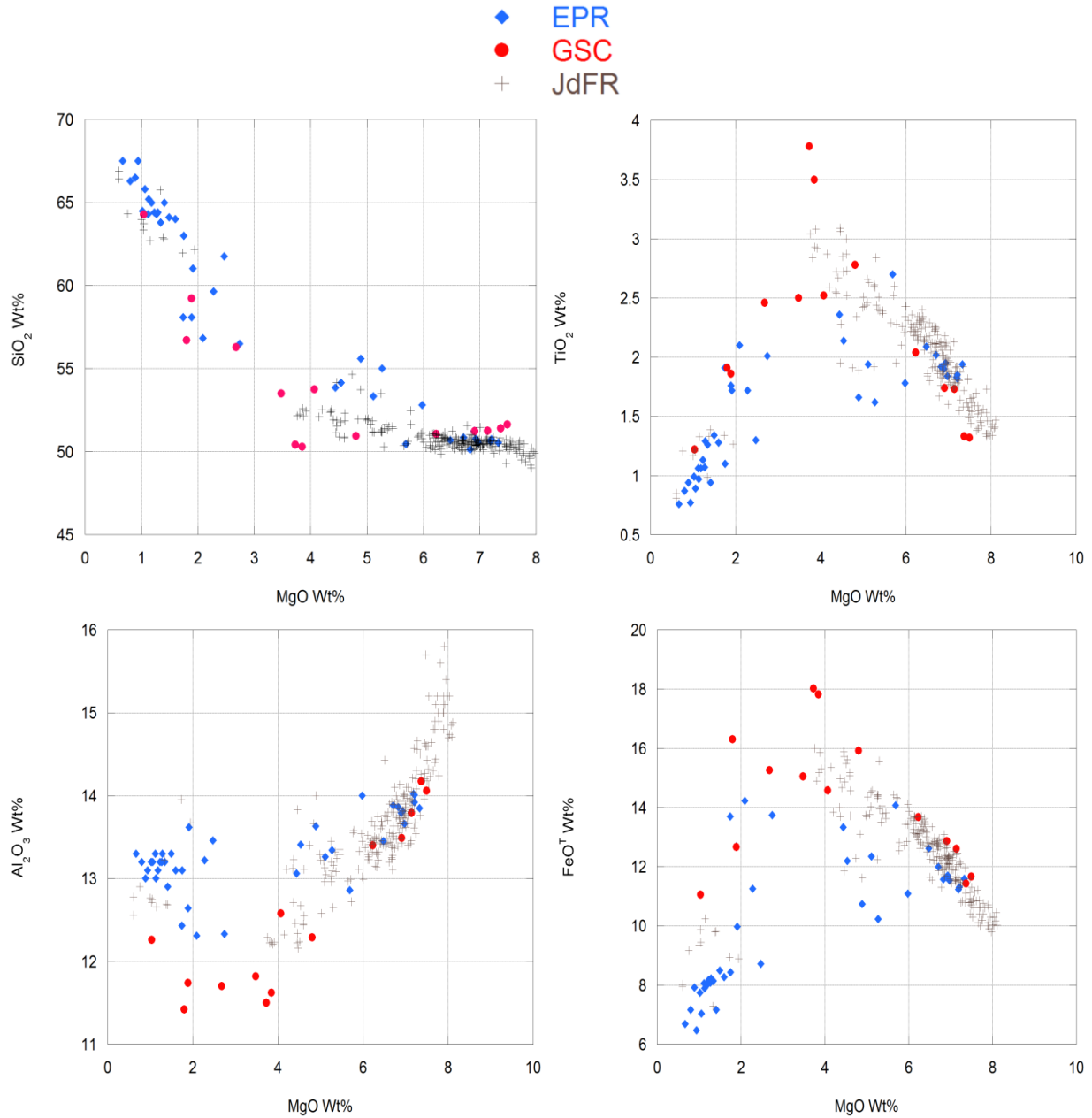


Figure 7-1. Major element variations for lavas from the 9°N OSC on the EPR (Wanless et al. 2010), 85°W GSC (Perfit et al. 1983) and the southern JdFR (Stakes et al. 2006 and this study). MgO is plotted against A) SiO₂, B) TiO₂, C) Al₂O₃ D) FeO(t) E) CaO F) Na₂O G) K₂O and H) P₂O₅

◆ EPR
● GSC
+ JdFR

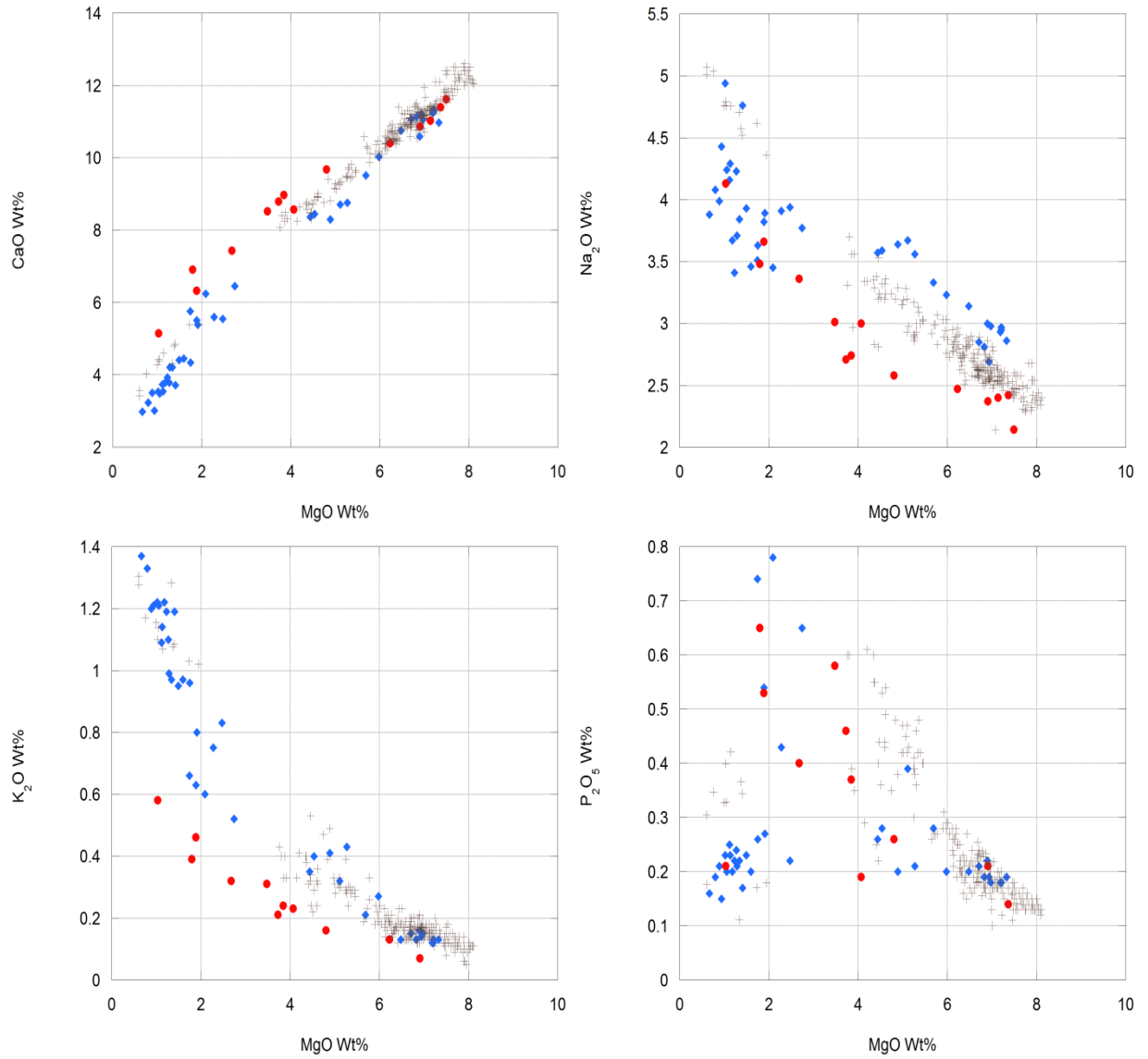


Figure 7-1. Continued

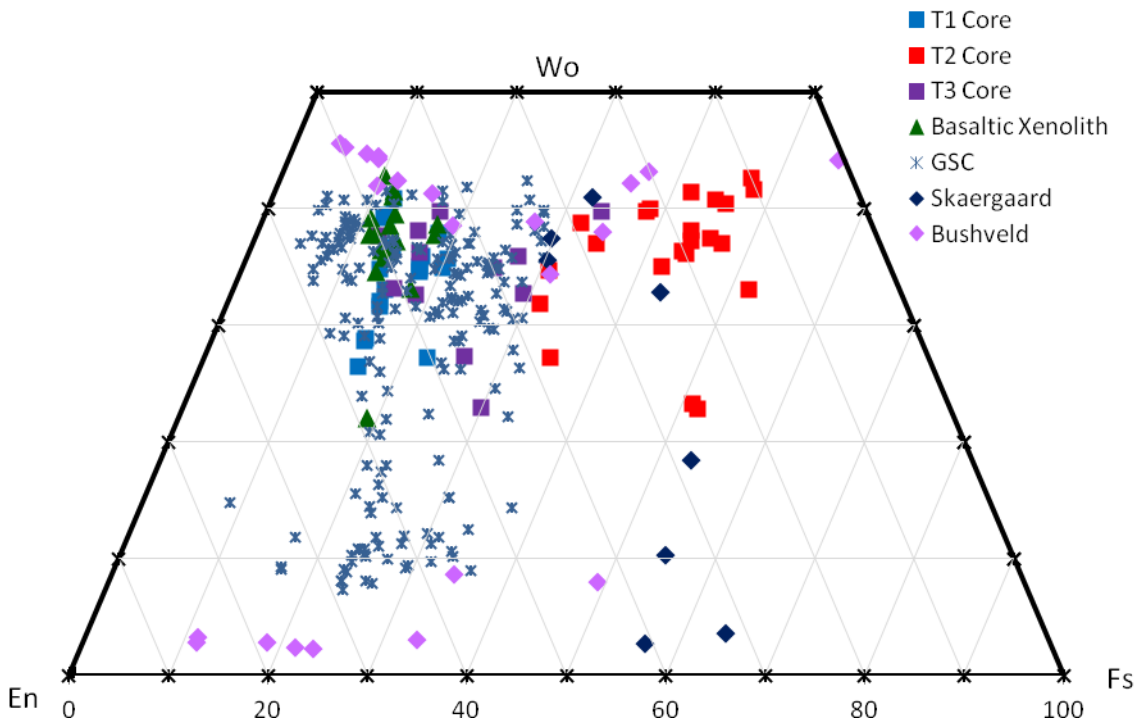


Figure 7-2. Pyroxene quadrilateral comparing T735 pyroxene trends with other tholeiitic suites. These suites include the GSC (Perfit et al. 1983 and Perfit unpublished) lavas and the Skaergaard (Nwe, 1975) and Bushveld (Atkins, 1969) complexes. Several pyroxenes plot within the pyroxene miscibility gap; possible reasons are discussed in the text.

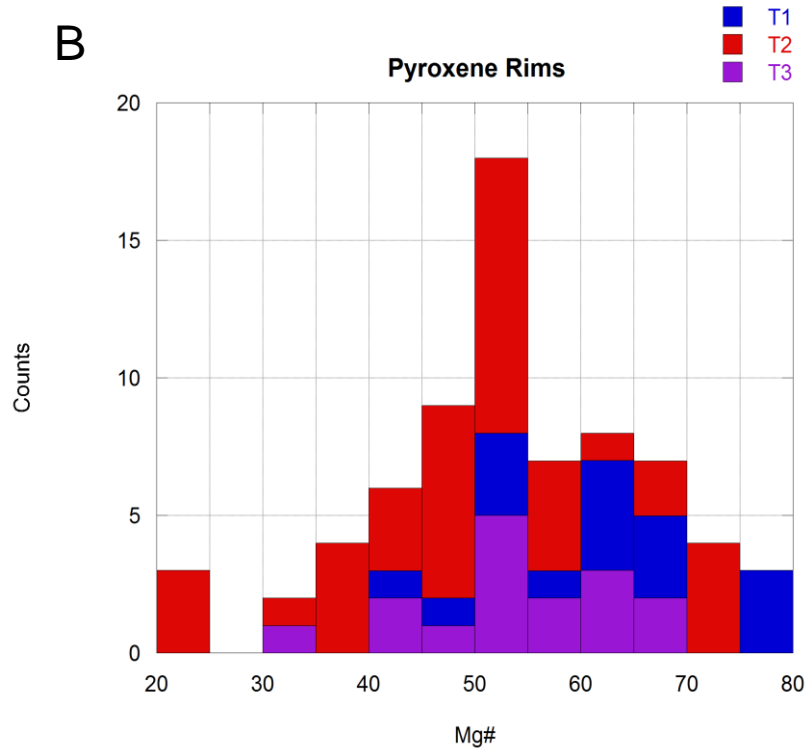
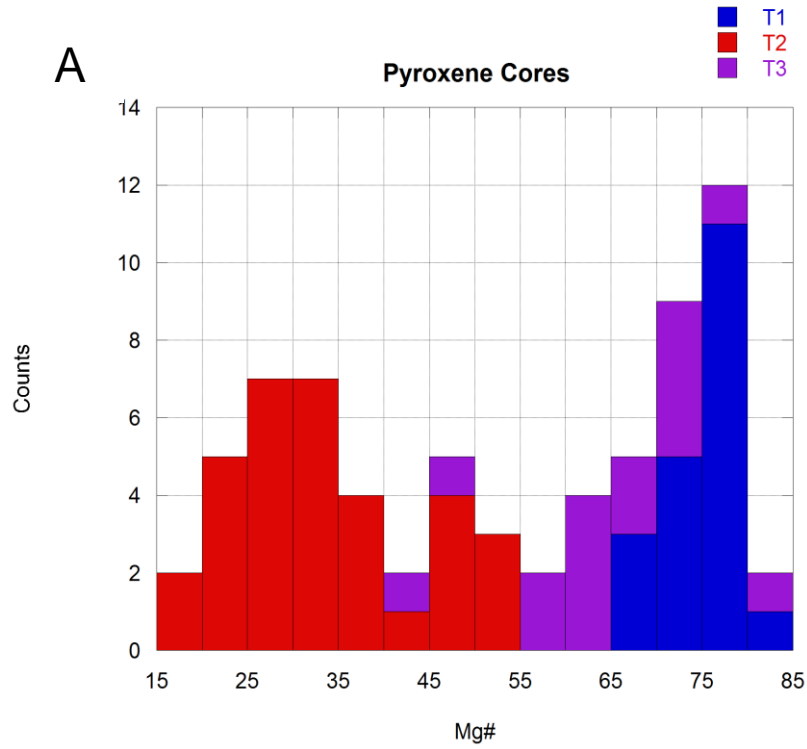


Figure 7-3. Histograms of pyroxene core and rim Mg#s. Analyses of type 1, 2, and 3 pyroxenes in A) cores and B) rims

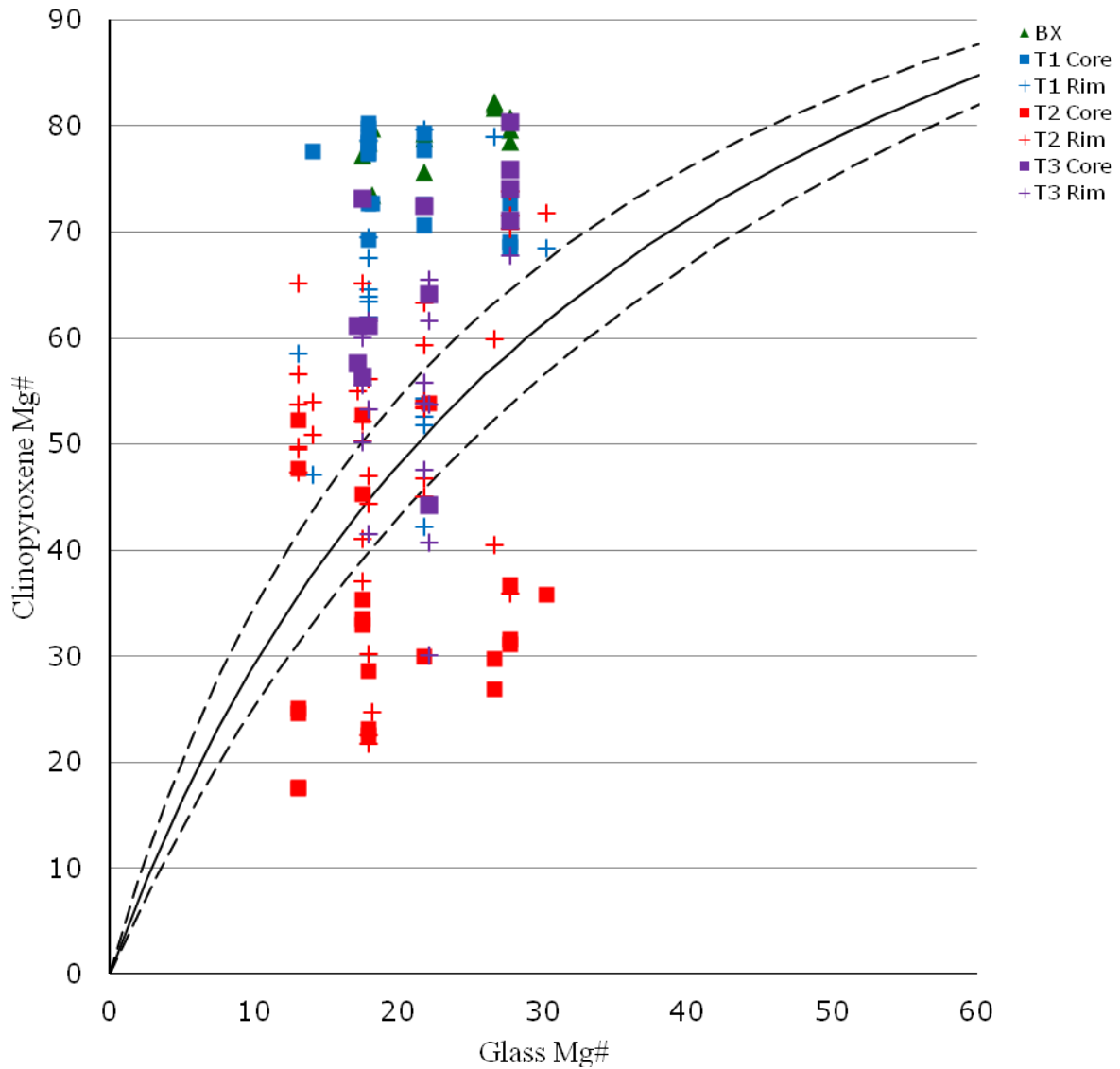


Figure 7-4. Pyroxene equilibria diagram based on Fe-Mg partitioning between clinopyroxene and liquid. The dashed lines represent the outer K_d boundaries of 0.24 and 0.30 with the solid line representing a K_d of 0.27. Pyroxene cores generally fall outside of the equilibrium envelope, however, many of the rims appear to be in equilibrium.

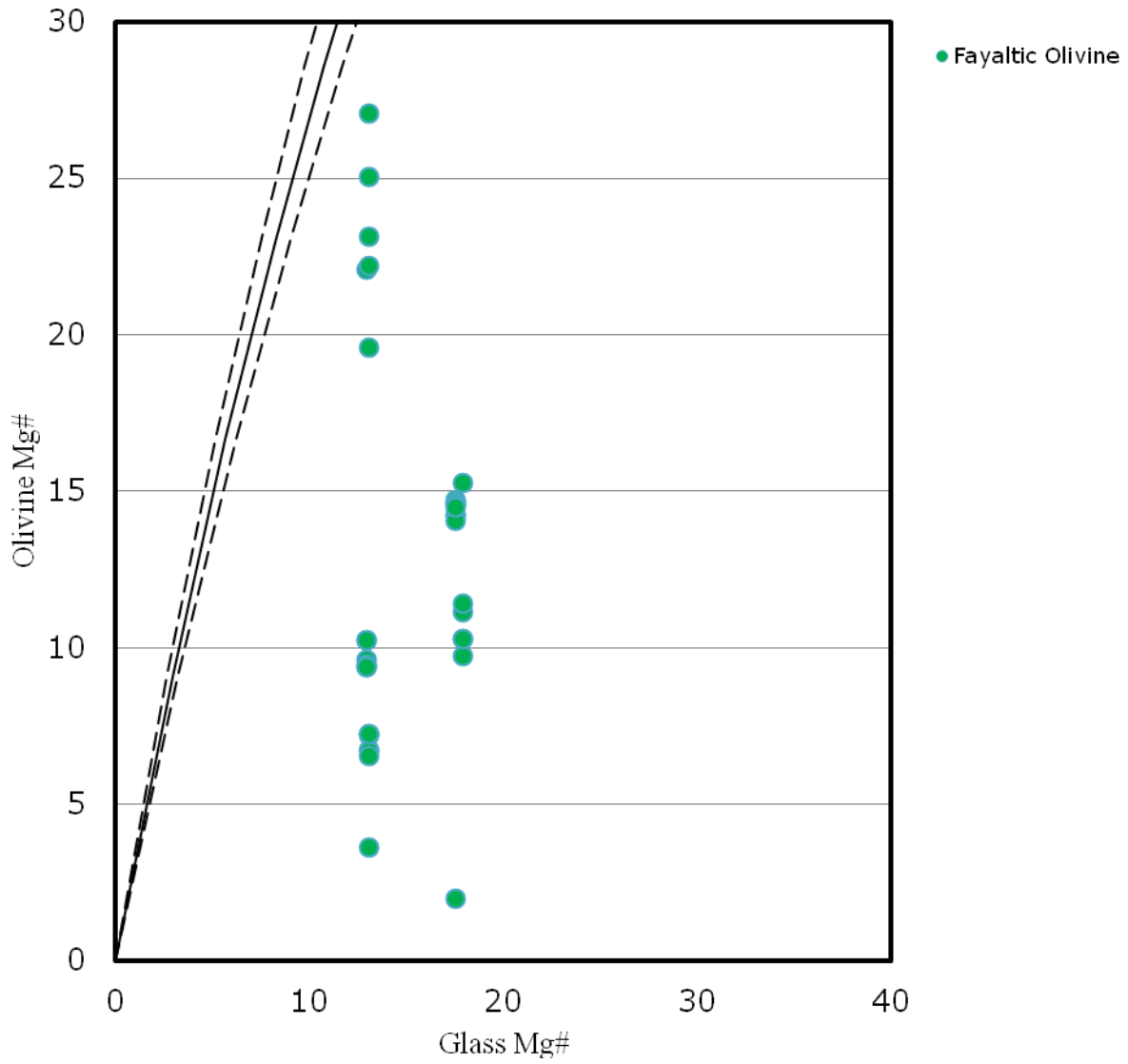


Figure 7-5. Olivine equilibria diagram based on Fe-Mg partitioning between olivine and liquid. The dashed lines represent the outer K_d boundaries of 0.27 and 0.33 with the solid line representing a K_d of 0.3.

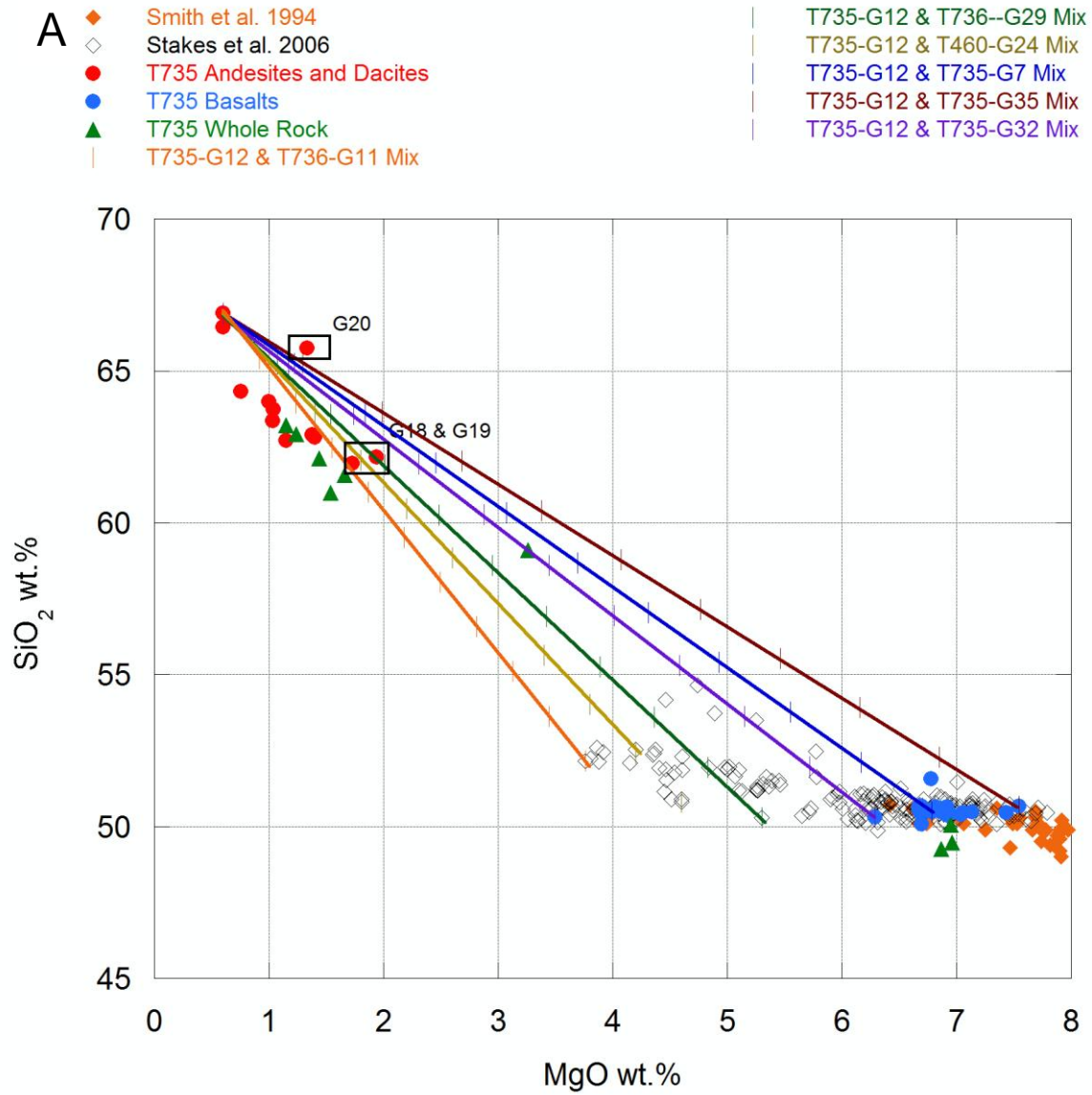


Figure 7-6. Mixing lines between sample G12 and various basaltic lavas for MgO vs. A) SiO₂ B) TiO₂ C) FeO(t) D) Na₂O E) K₂O and F) P₂O₅. The black arrow in C) indicates the direction of pyroxene fractionation.

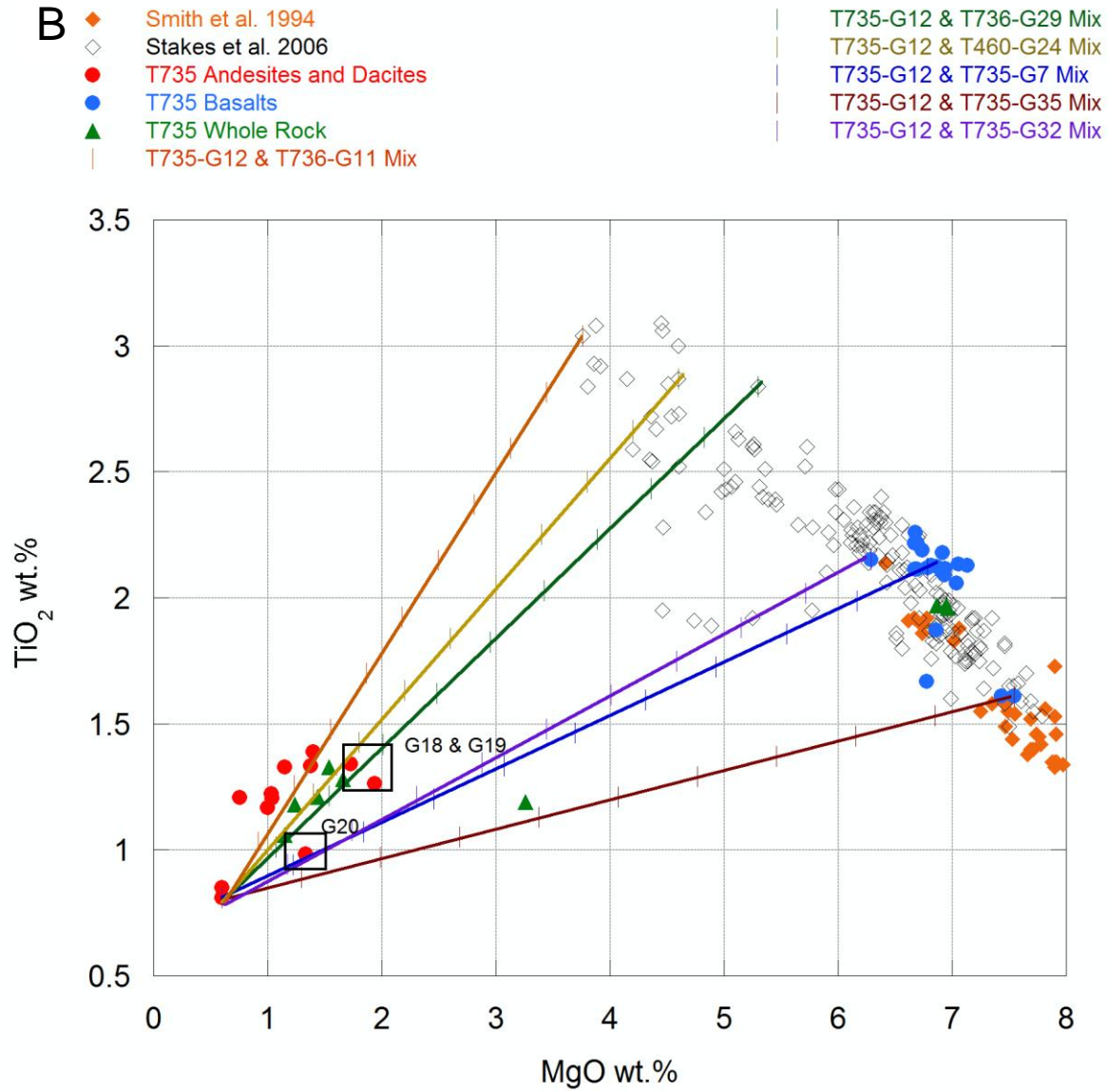


Figure 7-6. Continued

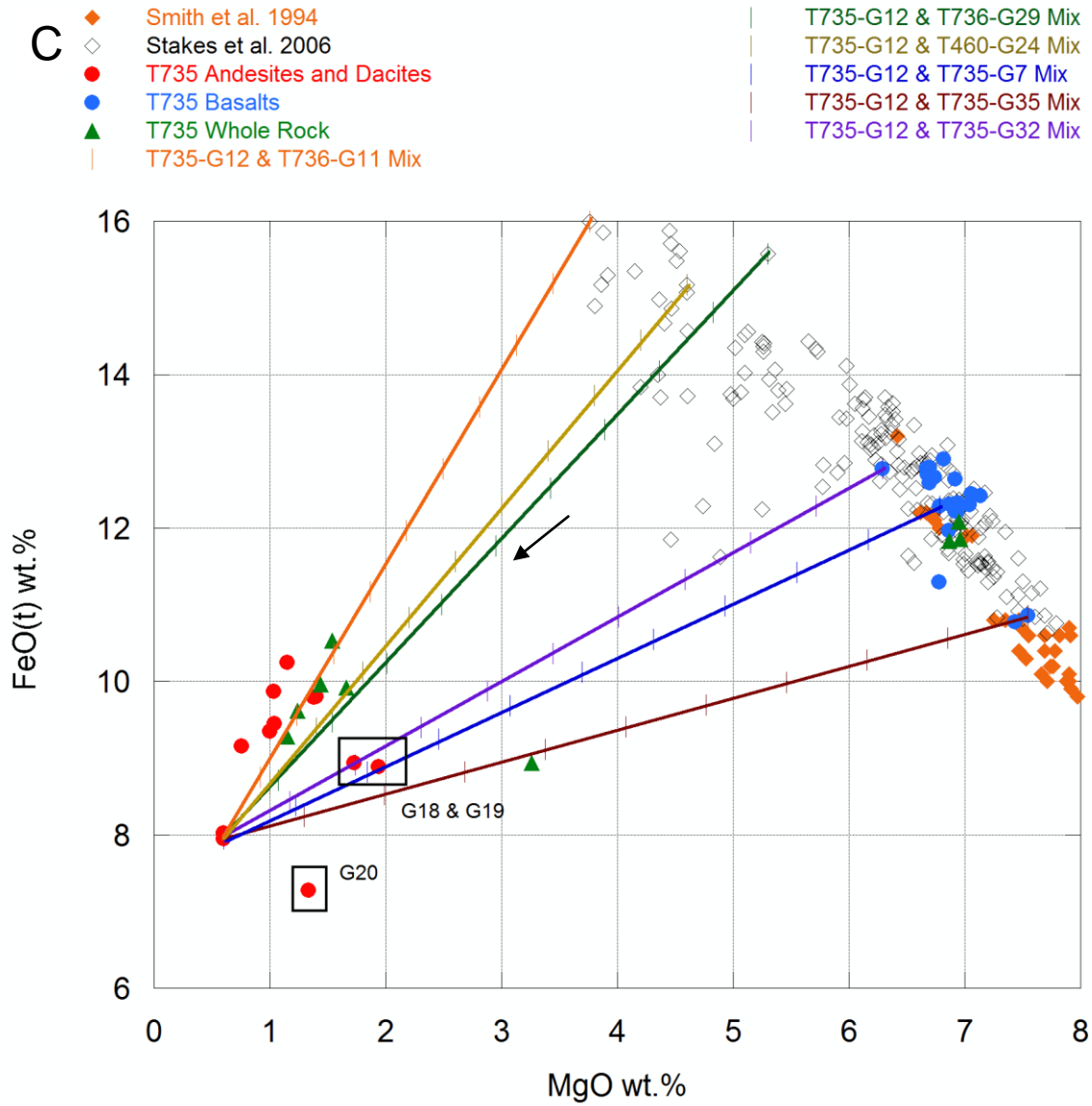


Figure 7-6. Continued.

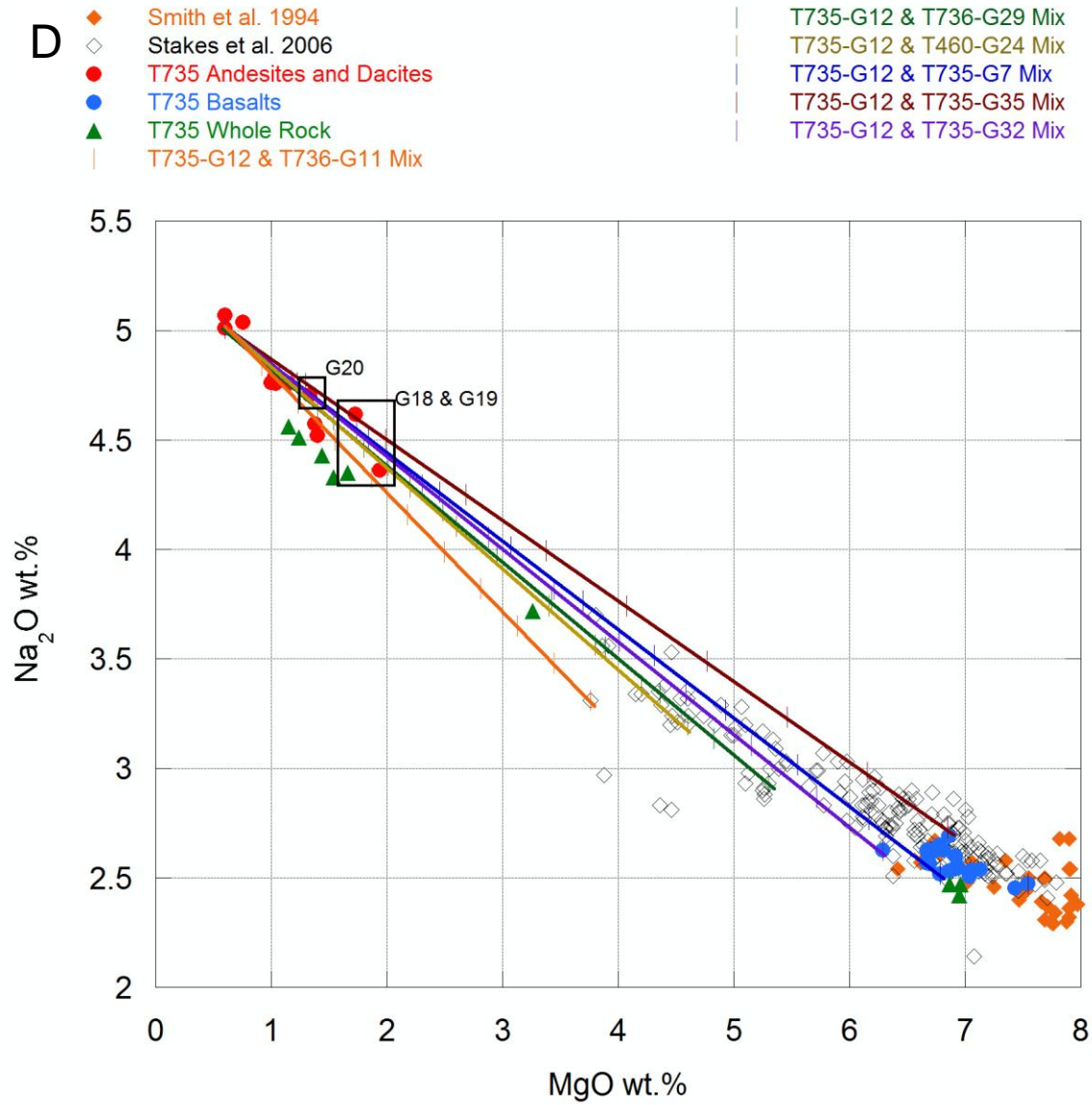


Figure 7-6. Continued.

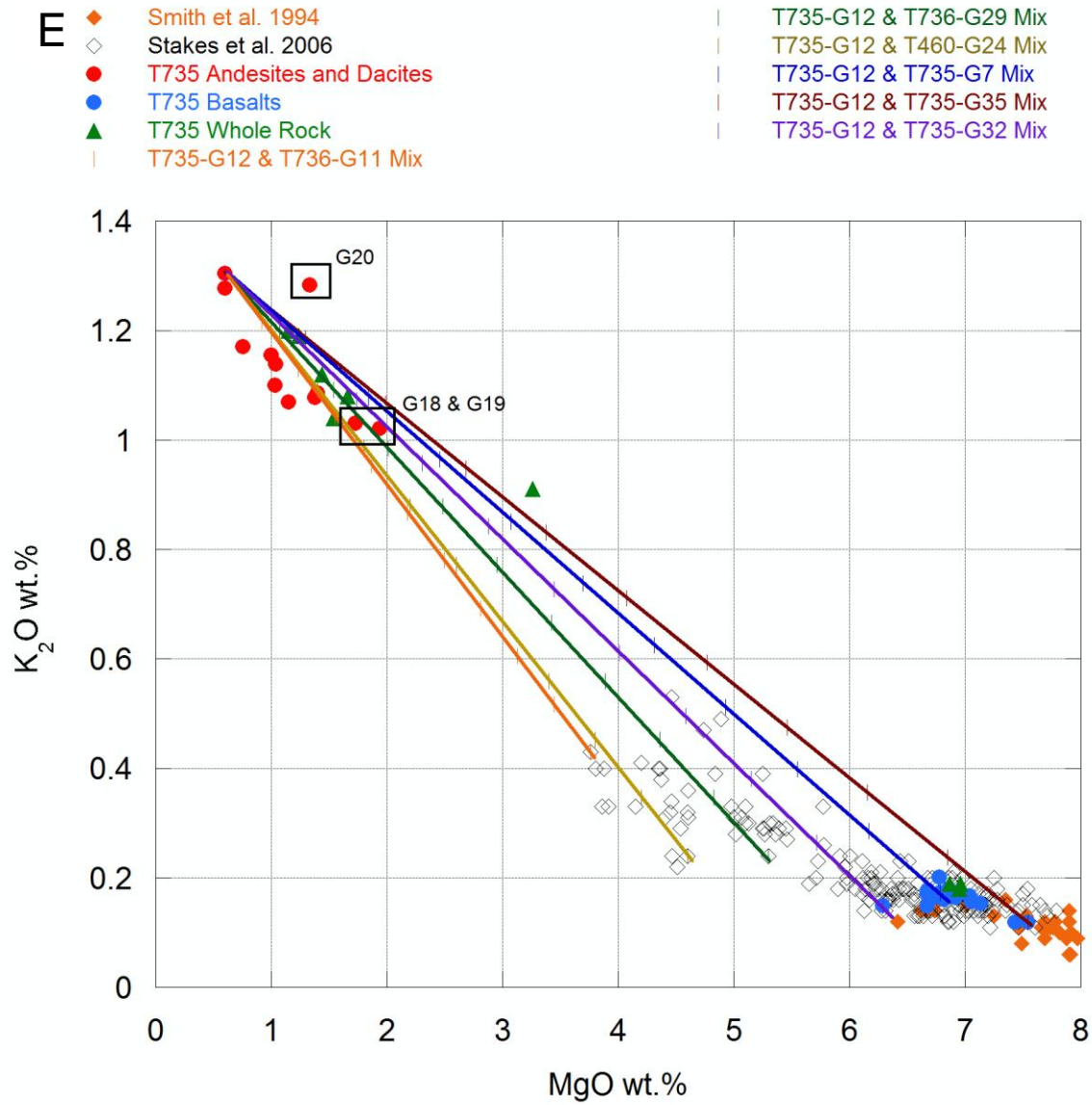


Figure 7-6. Continued

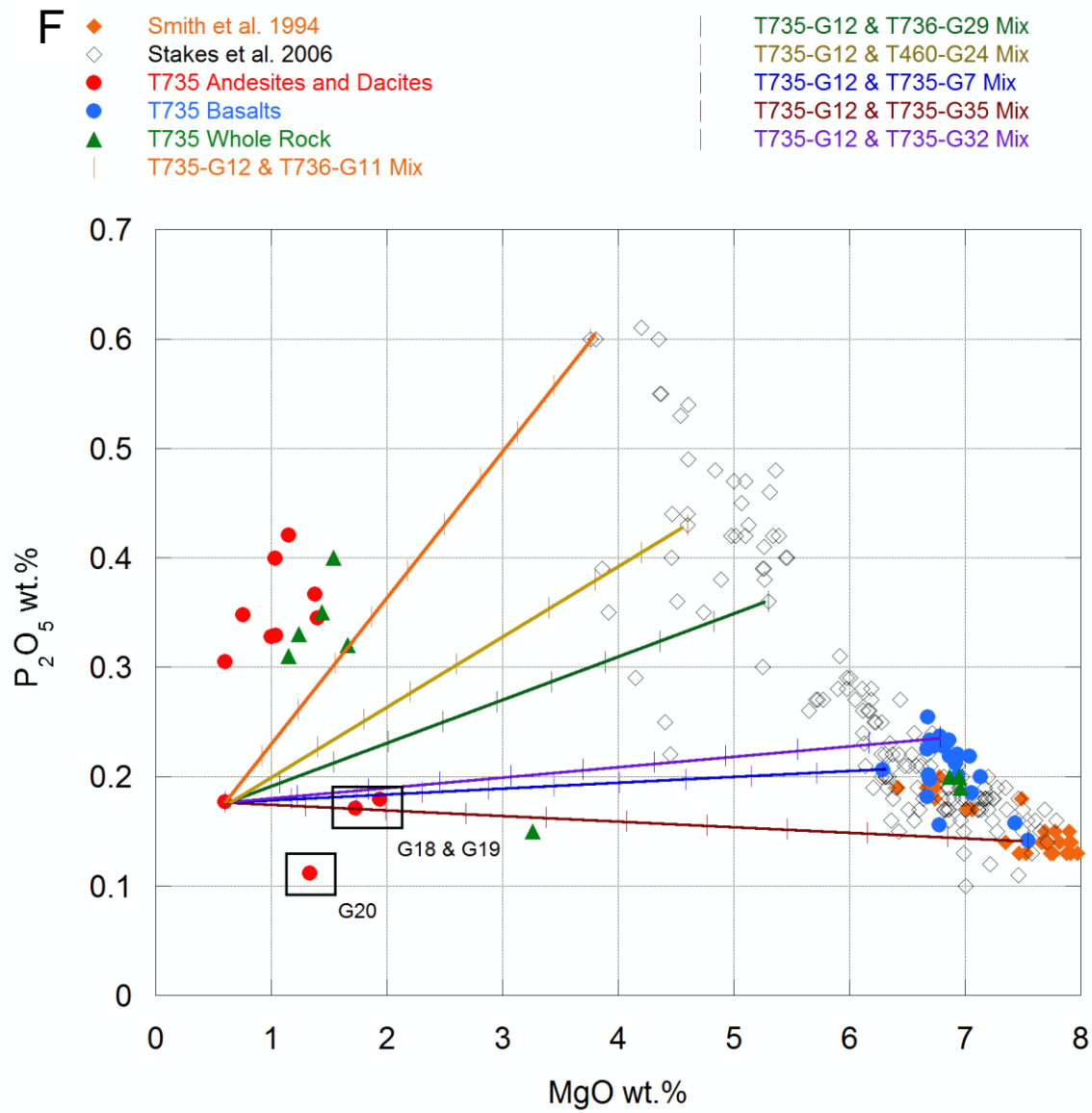


Figure 7-6. Continued

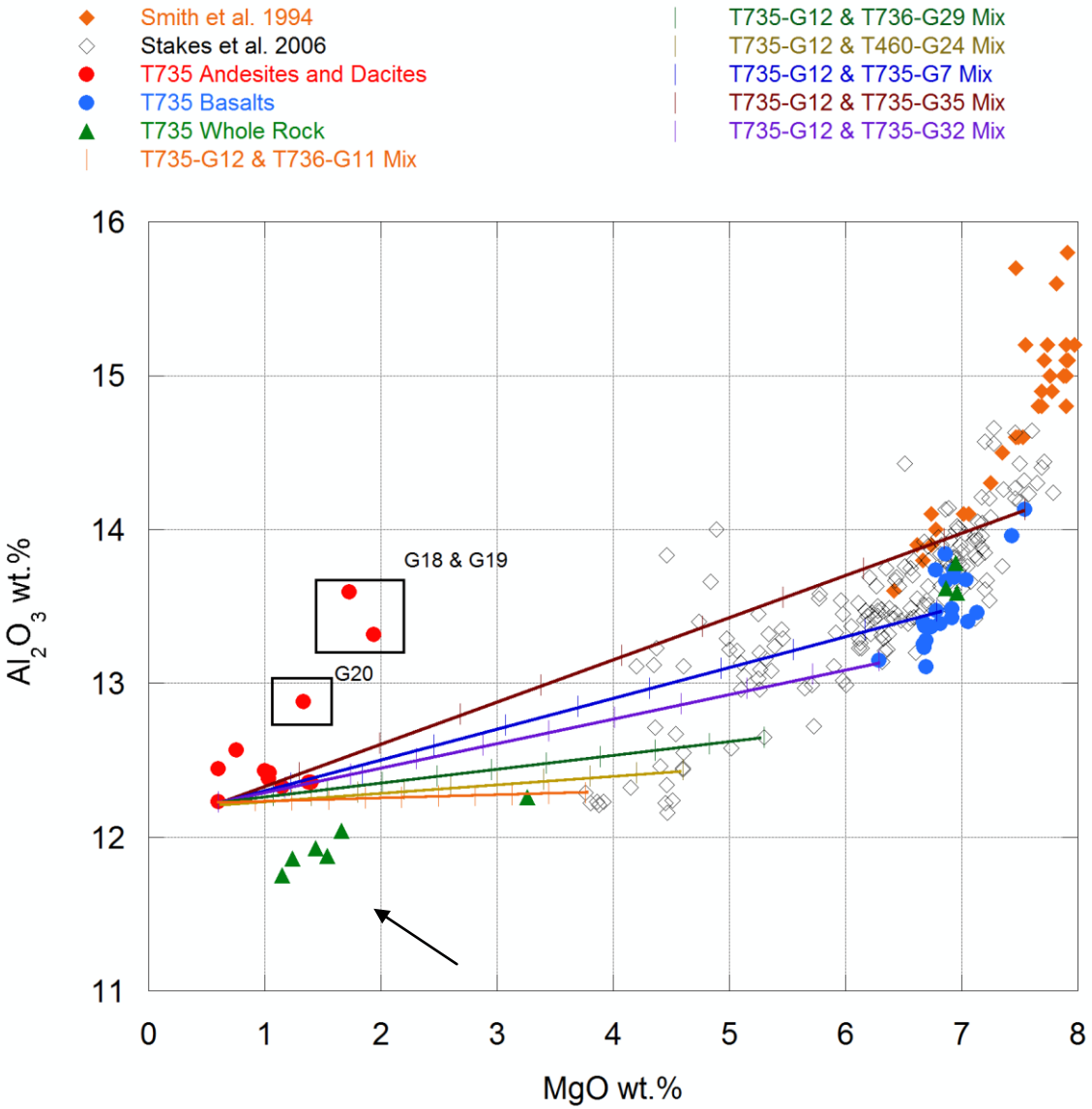


Figure 7-7. Mixing lines between sample G12 and various basaltic lavas for MgO (wt.%) vs. Al₂O₃ (wt.%). The black arrow indicates the direction of pyroxene fractionation.

CHATER 8 CONCLUSIONS

Dacitic lavas collected from mid-ocean ridge axis discontinuities have recently been attributed to extreme crystal fractionation with small amounts (5-20%) of partial melting and assimilation of hydrated oceanic crust. However, dacitic lavas from the ridge transform intersection of the Blanco Fracture Zone and southern Juan de Fuca Ridge indicate that magma mixing plays an important role in their evolution. The phyric nature and preservation of highly evolved mineral phases make this suite of dacites unique among those previously analyzed from RAD's. Assimilation of a plagiogranite source is required to explain the presence of highly evolved mineral phases (e.g. fayalitic olivine, quartz, Fe-rich pyroxene) and the presence of exsolved pyroxene and myrmekite. Mixing of 10-40% of a highly evolved basaltic magma such as FeTi basalt or basaltic andesite and partial melts from a plagiogranite source are able to reproduce most major element compositions. High Al_2O_3 values are attributed to the crystallization of pyroxene in the absence of plagioclase. In order to explain the high Cl/ K_2O ratios in the dacitic lavas; the plagiogranite source must either be hydrothermally altered or some assimilation must take place with saline brines in the oceanic crust.

LIST OF REFERENCES

- Atkins, F.B. (1969). "Pyroxenes of the Bushveld Intrusion, South Africa." *Journal of Petrology*. **10** (2): 222-249.
- Beard, J.S. & Lofgren, G. E. (1991). "Dehydration melting and water saturated melting of basaltic and andesitic greenstones and amphibolites at 1, 3, and 6.9 kb." *Journal of Petrology* **32**: 365-401.
- Bowen, N.L. (1928). *The Evolution of the Igneous Rocks*. Dover Publications, New York.
- Byerly, G. R., Melson, W. G., & Vogt, P. R. (1976). "Rhyodacites, andesites, ferro-basalts and ocean tholeiites from the Galapagos spreading center." *Earth Planet. Sci. Lett.* **30**: 215-221.
- Byerly, G. (1980). "The Nature of Differentiation Trends in Some Volcanic Rocks from the Galapagos Spreading Center." *Journal of Geophysical Research* **85**(87): 3,797-3,810.
- Canales, J. P., Detrick, R. S., Carbotte, S. M., Kent, G. M., Diebold, J. B., Harding, A., Babcock, J., Nedimovic, M. R. & Ark, E. V. (2005). "Upper crustal structure and axial topography at intermediate spreading ridges: Seismic constraints from the southern Juan de Fuca Ridge." *Journal of Geophysical Research* **110**.
- Chadwick, J., Perfit, M., Ridley, I., Jonasson, I., Kamenov, G., Chadwick, W., Embley, R., Le Roux, P., & Smith, M. (2005). "Magmatic effects of the Cobb hot spot on the Juan de Fuca Ridge." *Journal of Geophysical Research* **110**.
- Christie, D. M. & Sinton, J. M. (1981). "Evolution of abyssal lavas along propagating segments of the Galapagos spreading center." *Earth Planet. Sci. Lett.* **56**: 321-335.
- Clague, D. A. & Bunch, T. E. (1976). "Formation of Ferrobasalt at East Pacific Midocean Spreading Centers." *Journal of Geophysical Research* **81**(23): 4247-4256.
- Clague, D. A., Frey, F. A., Thompson, G., & Rindge, S. (1981). "Minor and trace element geochemistry of volcanic rocks dredged from the Galapagos spreading center: Role of crystal fractionation and mantle heterogeneity." *Journal of Geophysical Research* **86**: 9469-9482.
- Cotsonika, L. (2006). *Petrogenesis of Andesites and Dacites from the Southern Juan de Fuca Ridge*. *Geology*. Gainesville, University of Florida: 188 p.
- Crane, K., Aikman III, F., Embley, R., Hammond, S., & Malahoff, A. (1985). "The distribution of geothermal fields on the Juan de Fuca Ridge," *Journal of Geophysical Research* **90**: 727-744.

- Delaney, J. R., Johnson, H. P., & Karston, J. L. (1981). "The Juan de Fuca Ridge - hot spot- propagating rift system: New tectonic geochemical, and magnetic data." *Journal of Geophysical Research* **86**: 11,747-11,750.
- Embley, R. W., Hammond, S., Malahoff, A., Ryan, W. B. F., Crane, K., & Kappel, E. (1983). "Rifts of the southern Juan de Fuca." *Eos Trans. AGU* **64**: 853.
- Embley, R. W., Chadwick, W., Perfit, M. R., & Baker, E. T. (1991). "Geology of the northern Cleft segment, Juan de Fuca Ridge: Recent lava flows, sea-floor spreading, and the formation of megaplumes." *Geology* **19**: 771-775.
- Embley, R.W. and D.S. Wilson (1992). "Morphology of the Blanco Transform Fault Zone—NE Pacific: Implications for its tectonic evolution." *Marine Geophysical Researches*, **14**: 25-45.
- Embley, R. W., Chadwick, W., Perfit, M. R., Smith, M. C., & Delaney, J. R.(2000). "Recent eruptions on the CoAxial segment of the Juan de Fuca Ridge: Implications for mid-ocean ridge accretion processes". *Journal of Geophysical Research* **105**: 16501-16525.
- Fornai, D. J., Perfit, M. R., Malahoff, A., & Embley, R. (1983). "Geochemical studies of abyssal lavas recovered by DSRV Alvin from Eastern Galapagos Rift, Inca Transform, and Ecuador Rift 1. Major element variations in natural glasses and spacial distribution of lavas." *Journal of Geophysical Research* **88**: 10,519-10,529.
- Frey, H. M. & Lange, R. A. (2011). "Phenocryst complexity in andesites and dacites from the Tequila volcanic field, Mexico: Resolving the effects of degassing vs. magma mixing." *Contrib. Mineral. and Petrol.* **162**: 415-445.
- Gardner, J.E., Rutherford, M., Carey, S., & Sigurdsson, H. (1995). "Experimental constraints on pre eruptive water contents and changing magma storage prior to explosive eruptions of Mount St. Helens volcano." *Bull Volcano* **157**:1–17.
- Goss, A. R., Perfit, M. R., Ridley, W. I., Rubin, K. H., Kamenov, G. D., Soule, S. A., Fundis, A., & Fornari, D. J. (2010). "Geophysical of lavas from the 2005-2006 eruption at the East Pacific Rise, 9'46'N-9'56'N: Implications for ridge crest plumbing and decadal changes in magma chamber compositions." *Geochemistry, Geophysics, Geosystems* **11**(5): 1-35.
- Grove, T. L. & Juster, T.C. (1989). "Experimental investigations of low-Ca pyroxene stability and olivine-pyroxene-liquid equilibria at 1 atm in natural basaltic and andesitic liquids." *Contrib. Mineral. Petrol.* **103**: 287-305.
- Grove, T.L., Elkins-Tanton, L.T., Parman, S.W., Chatterjee, N., Muntener, O., & Gaetani, G.A. (2003). "Fractional crystallization and mantle-melting controls on calc-alkaline differentiation trends." *Contrib. Mineral. Petrol.* **145**: 515–533.

- Haase, K. M., Stroncik, N. A., Stroncik, N. A., Hekinian, R., & Stoffers, P. (2005). "Nb-depleted andesites from the Pacific-Antarctic Rise as analogs for early continental crust." *Geology* **33**(12): 921-924.
- Hekinian, R., Stoffers, P., Devey, C., Ackerman, D., Hemond, C., O'Connor, J., Binard, N., & Maia, M. (1997). "Intraplate versus ridge volcanism on the Pacific-Antarctic Ridge near 37°S-111°W." *Journal of Geophysical Research* **102**: 12,265-12,286.
- Hekinian, R., Stoffers, P., Ackerman, D., Revillon, S., Maia, M., & Bohn, M. (1999). "Ridge-hotspot interaction: the Pacific Antarctic Ridge and the foundation seamounts." *Marine Geology* **160**: 199-223.
- Johnson, E.R., Wallace, P., Delgado Granados, H., Manea, V.C., Kent, A.J.R., Bindeman, I.N., Donegan, C.S. (2009). "Subduction-related volatile recycling and magma generation beneath Central Mexico: insights from melt inclusions, oxygen isotopes and geodynamic models". *Journal of Petrology* **50**, 1729–1764.
- Juster, T. C., Grove, T. L., & Perfit, M. R. (1989). "Experimental constraints on the generation of FeTi basalts, andesites, and rhydacites at the Galapagos spreading center, 85°W and 95°W." *Journal of Geophysical Research* **94**: 9,251-9,274.
- Kappel, E. S., & Ryan, W. B. F. (1986). "Volcanic Episodicity and a Non-Steady State Rift Valley Along Northeast Pacific Spreading Centers: Evidence from Sea MARC 1." *Journal of Geophysical Research* **91**(B14): 13,925-13,940.
- Kinzler, R.J., & Grove, T.L. (1992). "Primary magmas of mid-ocean ridge basalts: 1. Experiments and methods." *Journal of Geophysical Research* **97**: 6,885-6,906.
- Koepke, J., Feig, S. T., Snow, J., & Freise, M. (2004). "Petrogenesis of oceanic plagiogranites by partial melting of gabbros: an experimental study." *Contrib. Mineral. Petrol.* **146**: 414-432.
- Kvassnes, A. J. S. & Grove, T. L. (2008). "How partial melts of mafic lower crust affect ascending magmas at oceanic ridges." *Contrib. Mineral. Petrol.* **156**: 49-71.
- Langmuir, C.H., Bender, J.F., Batiza, R. (1986). "Petrological and tectonic segmentation of the East Pacific Rise, 5°30'-14°30'N." *Nature* **322**: 422-429
- Mazzullo, L. J., & Bence, A. E. (1976). "Abyssal tholeiites from DSDP leg 34: The Nazca plate." *Journal of Geophysical Research* **81**: 4,327-4,351.
- Normark, W. R., Morton, J. L., Koski, R. A., Clague, D. A., & Delaney, J. R. (1983). "Active hydrothermal vents and sulfide deposits on the southern Juan de Fuca Ridge." *Geology* **11**: 158-163.
- Normark et al. (1986). "Submarine fissure eruptions and hydrothermal vents on the southern Juan de Fuca Ridge: Preliminary observations from the submersible Alvin: U.S. Geological Survey Juan de Fuca Study Group." *Geology* **14**: 823-827.

- Normark, W. R., Morton, J. L., & Ross, S. L. (1987). "Submersible Observations Along the Southern Juan de Fuca Ridge: 1984 Alvin Program." *Journal of Geophysical Research* **92**(B11): 11,283-11,290.
- Nwe, Y. Y. (1975). "Two Different Pyroxene Crystallisation Trends in the Trough Bands of the Skaergaard Intrusion, East Greenland." *Contrib. Mineral. Petrol.* **49**: 285-300.
- Pearce, T. H., Russel, J. K., & Wolfson, I. (1987). "Laser-interferences and Normarski interference imaging of zoning profiles and plagioclase phenocrysts from the May 18, 1980 eruption of Mount St. Helens, Washington." *Am. Mineral.* **72**: 1,131-1,143.
- Perfit, M. R. & Fornai, D. J. (1983). "Geochemical studies of abyssal lavas recovered by DSRV Alvin from eastern Galapagos Rift, Inca Transform, and Ecuador Rift 2. Phase chemistry and crystallization history." *Journal of Geophysical Research* **88**: 10,530-10,550.
- Perfit, M. R., Fornari, D. J., Malhoff, A., & Embley, R. W. (1983). "Geochemical studies of abyssal lavas recovered by DSRV Alvin from eastern Galapagos Rift, Inca Transform, and Ecuador Rift 3. Trace element abundances and petrogenesis." *Journal of Geophysical Research* **88**: 10,551-10,572.
- Perfit, M. R., and W. W. Chadwick, Jr., "Magmatism at mid-ocean ridges: Constraints from volcanological and geochemical investigations, in Faulting and Magmatism at Mid-Ocean Ridges", *Geophys. Monograph* **106**: 59-116.
- Raff, A.D., & Mason, P. G. (1961). "Magnetic survey off the west coast of North America, 40°N latitude to 52°N latitude." *Geological Society American Bulletin* **72**: 1,267-1,270.
- Regelous, M., Niu, Y., Wendt, J. I., Batiz, R., greig, A., & Collerson, K. D. (1999). "Variations in the geochemistry of magmatism on the East Pacific Rise at 10'30'N since 800 ka." *Earth Planet. Sci. Lett.* **168**: 45-63.
- Roeder, P. L. and R. F. Emslie (1970). "Olivine-Liquid Equilibrium." *Contr. Mineral. and Petrol.* **29**: 275-289.
- Rubin, K. H. & Sinton, J. M. (2007). "Inferences on mid-ocean ridge thermal and magmatic structure from MORB compositions." *Earth Planet. Sci. Lett.* **260**: 257-276.
- Schmitt, A. K., Perfit, M. R., Rubin, K. H., Stockli, D. F., Smith, M. C., Cotsonika, L. A., Zellmer, G. F., Ridley, W. I., & Lovera, O. M. (2011). "Rapid cooling rates at an active mid-ocean ridge from zircon thermochronology." *Earth Planet. Sci. Lett* **302**: 349-358.

- Shelley, David, 1993, *Igneous and Metamorphic Rocks Under the Microscope*, Chapman and Hall, London, UK
- Sinton, J. M. & Detrick, R. S. (1992). "Mid-ocean ridge magma chambers." *Journal of Geophysical Research* **97**. 197-216.
- Sinton, J. M., Wilson, D. S., Christie, D. M., Hey, R. N., & Delaney, J. R. (1983). "Petrologic consequences of rift propagation on oceanic spreading ridges." *Earth Planet. Sci. Lett.* **62**: 193-207.
- Smith, M. C., Perft, M. R., & Jonasson, I. R. (1994). "Petrology and geochemistry of basalts from the southern Juan de Fuca Ridge: Controls on the spatial and temporal evolution of mid-ocean ridge basalt." *Journal of Geophysical Research* **99**: 4,787-4,812.
- Stakes, D. S., Perfit, M. R., Tivey, M. A., Caress, D. W., Ramirez, T. M., & Maher, M. (2006). "The Cleft revealed: Geologic, magnetic, and morphologic evidence for constriction of upper oceanic crust along the southern Juan de Fuca Ridge." *Geochemistry, Geophysics, Geosystems* **7**(4): 1-32.
- Taylor, R. B. (1964). *Geology of the Duluth Gabbro Complex near Duluth, Minnesota*. The University of Minnesota Press, Minneapolis.
- Tierney, S. E. (2003) *Distribution and composition of lavas from the southern Cleft segment of the Juan de Fuca Ridge: Tectonomagnetic evolution of a ridge-transform intersection*. University of Florida: 195.
- Ussler III, W., Glazner, A.F. (1989) "Phase equilibria along a basalt-rhyolite mixing line: implications for the origin of calc-alkaline intermediate magmas". *Contrib. Mineral. Petrol.* **101**: 232-244.
- Vine, F. J., & Wilson, J. T. (1965). "Magnetic anomalies over a young oceanic ridge off Vancouver Island." *Science* **150**: 485-489.
- Vogt, P.R., Johnson, G.L. (1973) "Magnetic telechemistry of oceanic crust?" *Nature*. **245**: 373-375
- Wanless, V. D., Perfit, M. R., Ridley, W. I., & Klein, E. (2010). "Dacite petrogenesis on mid-ocean ridges: Evidence for oceanic crustal melting and assimilation." *Journal of Petrology* **51** (12): 2377-2410.
- Wanless, V.D., Perfit, M.R., Ridley, W.I., Wallace, P.J., Grimes, C.B., & Klein, E.M. (2011). "Volatile abundances and oxygen isotopes in basaltic to dacitic lavas on mid-ocean ridges: The role of assimilation at spreading centers." *Chemical Geology* **287**: 54-65.
- Wilson, J. T. (1965). "Transform faults, oceanic ridges and magnetic anomalies southwest of Vancouver Island." *Science* **150**: 482-485.

White, S. M., Mason, J. L., Macdonald, K. C., Perfit, M. R., Wanless, D. V., & Klein, E. M. (2009). "Significance of widespread low effusion rate eruptions over the past two million years for delivery of magma to the overlapping spreading centers at 9°N East Pacific Rise." *Earth Planet. Sci. Lett.* **280**: 175-184.

BIOGRAPHICAL SKETCH

Kevin Werts grew up in Lubbock, Texas and graduated from Frenship High School in the spring of 2004. He then attended South Plains Community college from the fall of 2004 to the spring of 2006. Afterwards, he attended Texas Tech University beginning in the summer of 2006 where he majored in geological sciences. He earned his B.S. in geology in the summer of 2010. Then he began graduate school at the University of Florida in the fall of 2010 and earned his M.S. in geology in the summer of 2012.